THE FORMATION AND EVOLUTION OF PLANETARY SYSTEMS: GRAIN GROWTH AND CHEMICAL PROCESSING OF DUST IN T TAURI SYSTEMS

J. BOUWMAN AND TH. HENNING
Max Planck Institute for Astronomy, Königstuhl 17, D-69117 Heidelberg, Germany

L. A. HILLENBRAND
Department of Astronomy, California Institute of Technology, Pasadena, CA 91125

M. R. MEYER AND I. PASCUCCI
Steward Observatory, University of Arizona, 933 North Cherry Avenue, Tucson, AZ 85721-0065

J. CARPENTER
Department of Astronomy, California Institute of Technology, Pasadena, CA 91125

D. HINES
Space Science Institute, 4750 Walnut Street, Suite 205, Boulder, CO 80301

J. S. KIM AND M. D. SILVERSTONE
Steward Observatory, University of Arizona, 933 North Cherry Avenue, Tucson, AZ 85721-0065

D. HOLLENBACH
NASA Ames Research Center, Moffet Field, CA 94035

AND

S. WOLF
Max Planck Institute for Astronomy, Königstuhl 17, D-69117 Heidelberg, Germany

ABSTRACT

This paper is one in a series presenting results obtained within the Formation and Evolution of Planetary Systems (FEPS) Legacy Science Program on the *Spitzer Space Telescope*. Here we present a study of dust processing and growth in seven protoplanetary disks. Our spectra indicate that the circumstellar silicate dust grains have grown to sizes at least 10 times larger than observed in the interstellar medium and show evidence for a non-negligible ($\sim$5% in mass fractions) contribution from crystalline species. These results are similar to those of other studies of protoplanetary disks. In addition, we find a correlation between the strength of the amorphous silicate feature and the shape of the spectral energy distribution. This latter result is consistent with the growth and subsequent gravitational settling of dust grains toward the disk midplane. Furthermore, we find a change in the relative abundance of the different crystalline species: more enstatite than forsterite is observed in the inner warm dust population at $\sim$1 AU, while forsterite dominates in the colder outer regions at $\sim$5–15 AU. This change in the relative abundances argues for a localized crystallization process rather than a radial mixing scenario in which crystalline silicates are being transported outwards from a single formation region in the hot inner parts of the disk. Finally, we report the detection of emission from polycyclic aromatic hydrocarbon (PAH) molecules in five out of seven sources. We find a tentative PAH band at 8.2 μm that was previously undetected in the spectra of disks around low-mass pre-main-sequence stars.

Subject headings: circumstellar matter — planetary systems — stars: pre–main-sequence

Online material: color figures

1. INTRODUCTION

The circumstellar disks surrounding pre-main-sequence brown dwarfs (BDs), T Tauri stars (TTSs), and Herbig Ae-Be (HAeBe) systems are believed to be the sites of ongoing planet formation (e.g., Luhman et al. 2007; Natta et al. 2007); from here on, we will refer to these disks as protoplanetary disks. As most of the youngest (<1 Myr) solar-mass stars have circumstellar disks (Strom et al. 1989) with typical masses (Beckwith et al. 1990) and sizes (McCaughrean & O'Dell 1996; Dutrey et al. 1996) comparable to the expected values for the primitive solar nebula, these disks are the natural candidates for the birth sites of planets. The submicron-sized dust grains initially present in these disks can coagulate to form larger objects and eventually Earthlike planets (e.g., Weidenschilling 1997; Henning et al. 2006). By deriving the composition of the circumstellar dust and identifying the processes governing its chemistry and coagulation, valuable insights can be gained into the workings of protoplanetary disks (e.g., Bouwman et al. 2001, 2003; van Boekel et al. 2003, 2005; Przygodda et al. 2003; Kessler-Silacci et al. 2006; Sargent et al. 2006), and thus the planet formation process. The results of these analyses can be compared directly with the investigation of solar system objects such as comets, meteorites, and interplanetary dust particles (IDPs), which preserve a record of the early phases in the evolution of the solar system.

With the *Infrared Astronomical Satellite* (*IRAS*) and *Infrared Space Observatory* (*ISO*) missions, a tremendous advance in our knowledge of protoplanetary disks has been achieved. However, the spectroscopic studies with these missions were limited to relatively nearby and luminous stars of spectral types A and B, and

TABLE 1
Astrophysical Parameters of Program Stars

ID	Name	R.A. (J. 2000)	Decl. (J. 2000)	d (pc)	log (Age) (yr)	Spectral Type	T_{eff} (K)	A_V (mag)	L_{star} ($L_\odot$)	Reference
0..........	RX J1842.9−3532	18 42 57.98	−35 32 42.73	145	6.63 (4 Myr)	K2	4995	1.03	1.0	2, 3, 1
1..........	RX J1852.3−3700	18 52 17.30	−37 00 11.93	145	6.5–7 (4 Myr)	K3	4759	0.92	0.6	2, 3, 1
2..........	HD 143006	15 58 36.92	−22 57 15.35	145	6.70 (5 Myr)	G6/8	5884	1.63	2.5	7, 8, 9
3..........	RX J1612.6−1859A (2MASS J16123916−1859284)	16 12 39.18	−18 59 28.0	145	6.70 (3 Myr)	M0	3800	1.80	0.5	11
4..........	1RXS J132207.2−693812 (PDS 66)	13 22 07.53	−69 38 12.18	86	7.23 (17 Myr)	K1I Ve	5228	1.22	1.3	10
5..........	RX J1111.7−7620	11 11 46.32	−76 20 09.21	163	6.69 (5 Myr)	K1	4621	1.30	1.6	5, 3, 4
6..........	1RXS J161410.6−230542 ([PZ99] J161411.0−230536)	16 14 11.08	−23 05 36.26	145	6.70 (5 Myr)	K0	4963	1.48	3.2	7, 8, 6

Notes.—Units of right ascension are hours, minutes, and seconds, and units of declination are degrees, arcminutes, and arcseconds. Spectral types are from optical spectroscopy as cited above. $B-V$ and $V-K$ colors are used in conjunction with spectral types to estimate effective temperatures and visual extinction values; see Carpenter et al. (2008) for details. In the case of RX J1612.6−1859A, $J-H$ and $H-K$ colors are used, and luminosity is computed from J-band bolometric correction.

References.—References for distance, age, and spectral type: (1) Neuhauser et al. 2000; (2) Neuhauser & Forbrich 2008; (3) L. A. Hillenbrand et al. 2008, in preparation; (4) Alcala et al. 1995; (5) Luhman 2008; (6) Preibisch et al. 1998; (7) de Zeeuw et al. 1999; (8) Preibisch et al. 2002; (9) Houk & Smith-Moore 1988; (10) Mamajek et al. 2002; (11) Martin et al. 1998.

provided only limited knowledge of the evolution of solar-mass systems. With the launch of the *Spitzer Space Telescope* (Werner et al. 2004), these less luminous systems have become accessible to observations. The FEPS *Spitzer* Legacy program probes the circumstellar dust properties around a representative sample of protoplanetary disks and debris disks, spanning a wide range of circumstellar disk properties and covering the major phases of planet system formation and evolution (Meyer et al. 2006)

We present an analysis of the infrared (IR) spectra of protoplanetary disks around seven pre-main-sequence systems observed within the FEPS legacy program. These are the only systems among the 328 FEPS targets that show spectroscopic features from solid-state dust components (see Meyer et al. 2006 for a detailed description of the FEPS parent sample). In Table 1, the astrophysical parameters of these seven stars are compiled. Five of the systems, RX J1842.9−3532, RX J1852.3−3700, 1RXS J132207.2−693812, RX J1111.7−7620, and 1RXS J161410.6−230542, were identified in Silverstone et al. (2006) as optically thick primordial disks on the basis of their IRAC colors and excess emission at wavelengths shorter than 8 μm. Silverstone et al. (2006) provide a literature review for the five stars identified in their study. In addition to these five systems, HD 143006 and RX J1612.6−1859A also show evidence for optically thick disks and solid-state features. We give a literature review for these two stars in Appendices A and B. HD 143006 was added to the FEPS sample on the basis of its *IRAS* excess emission in order to search for remnant gas in that system (e.g., Pascucci et al. 2006). The solid-state features in RX J1612.6−1859A were noticed from visual inspection of its spectrum. No other sources in the FEPS sample show evidence of solid-state emission features. Of these 321 sources, most lack excess in the *Spitzer* Infrared Spectrograph (IRS) wavelengths, and a few exhibit optically thin emission from debris. No other optically thick circumstellar disk sources are present in the data other than the seven with solid-state emission features discussed here.

We study the compositional properties of the systems listed in Table 1 using 5–35 μm spectra obtained with the IRS (Houck et al. 2004) on board the *Spitzer Space Telescope*. We focus on silicate grain processing (silicates make up the bulk of the refractory dust mass assuming solar system abundances) and perform a quantitative analysis of the observed solid-state emission. Using a consistent analysis method for the entire sample, the derived grain composition of the individual systems can be compared directly. This enables us look for signs of silicate grain processing. Apart from analyzing the 10 μm spectral region, which is also accessible to ground-based studies, *Spitzer* provides access to the silicate resonances at longer wavelengths. This enables us to study the dust composition of not only the warmest dust (∼500–1000 K), located in the inner parts (∼0.1–1 AU) of the protoplanetary disks around Sunlike stars, but also the cold (∼100 K) dust component in the outer regions (∼15 AU) of the disks.

This paper is organized in the following way. In § 2, we discuss the data reduction, introduce the main dust components, and present the method used to analyze the *Spitzer* IRS spectra. In § 3 modeling results are presented, and in § 4 we discuss implications for the evolution of the dust in the circumstellar disks around solar-mass stars.

2. OBSERVATIONS AND DUST MODELS

2.1. *The IRS Low-Resolution Spectra*

We obtained low-resolution ($R = \sim 60-120$) spectra with the IRS instrument on board *Spitzer*. A high-accuracy IRS or PCRS peak-up (with a 1 σ pointing uncertainty of 0.4″ radius) was used to acquire targets in the spectrograph slit, thus minimizing slit losses and assuring high photometric accuracy to about 10%. Two nod positions per cycle were obtained in standard staring mode with a minimum of six cycles per target for redundancy and to allow the rejection of artifacts introduced by bad pixels or cosmic-ray hits. The integration times were 6 and 14 s for the brightest and faintest sources, respectively. The targets were observed with the full spectral coverage of the IRS low-resolution instrument between 5.2 and 35 μm. Beyond 35 μm, the spectra suffer from excess noise (Houck et al. 2004) and cannot be used.

Our spectra are based on the droopres intermediate data product processed through the *Spitzer* Science Center (SSC) pipeline S12.0.2. Partially based on the SMART software package (see Higdon et al. 2004 for details on this tool and extraction methods), our data were further processed using spectral extraction tools developed for the FEPS *Spitzer* science legacy program. As a first step, we corrected for the background emission and stray light by subtracting the associated pairs of imaged spectra of the two nodded positions along the slit for each module and order. In this way, we also corrected for pixels that had an anomalous dark

current. Pixels flagged by the SSC data pipeline as "bad" were replaced with a value interpolated from an 8 pixel perimeter surrounding the errant pixel. We then extracted the spectra from the resulting set of images using a 6.0 pixel and a 5.0 pixel fixed-width aperture in the spatial dimension for the observations with the short- (5.2–14 μm) and long-wavelength (14–35 μm) modules, respectively. The low-level fringing at wavelengths >20 μm was removed using the irsfringe package (Lahuis & Boogert 2003).

Absolute flux calibration was achieved in a self-consistent manner using the ensemble of FEPS observations. As the majority of the 328 FEPS program stars exhibit stellar photospheres throughout the shorter wavelength range of the IRS, this data set is unique for calibrating the IRS instrument. From our full set of FEPS observations, we selected a subset of the spectra that complied with the following criteria: (1) colors (24–33 μm) within 1 σ of an extrapolated best-fit model photosphere (e.g., Meyer et al. 2004; Carpenter et al. 2006), and (2) a signal-to-noise ratio (S/N) larger than 50 with no artifacts within the spectra. This resulted in a set of 16 stars for the first order of the short-wavelength module (SL1) and the long-wavelength module spectra (LL1, LL2) and in a subset of 10 stars for the shorter wavelength orders (SL2). Together with the stellar photospheric models for these two subsets, we used these spectra to derive the relative spectral response functions (RSRFs) for the absolute flux calibration. For the relative (point-to-point) calibration, we derived RSRFs using six calibration stars observed at different epochs that have superior S/Ns and for which Cohen photospheric models are provided by the SSC. This procedure ensures that the RSRFs used to calibrate our protoplanetary disk spectra have the highest possible S/N and an estimated absolute flux calibration uncertainty of ~10%. For further details on the flux calibration, see the explanatory supplement for the FEPS data, delivered to the *Spitzer* data archive.

The resulting calibrated spectral energy distributions are shown in Figure 1. A detailed view of these spectra in three wavelength bands, showing more clearly the solid-state emission features, is presented in Figure 2. As one can see from Figure 1, a wide range in spectral shape and emission feature strength can be observed. In the next section, we will discuss the analysis methods and the different silicate components and grain models used to interpret the spectra shown in Figure 2.

2.2. *Outline of Spectral Analysis Methods*

For the analysis and interpretation of our observations, we use a two-fold approach. First, we characterize the spectra by measuring the strengths and positions of spectral features. Second, we decompose the observed emission features to determine the relative contributions of different silicate grains. For the spectral characterization, we employ a method similar to schemes previously used to analyze IR spectra from the *ISO* (e.g., Molster et al. 2002a, 2002b) and ground-based observations (e.g., van Boekel et al. 2005). To measure the emission band strengths and positions, we first fit a low-order polynomial (second order in the 10 μm region, fifth order for $\lambda > 15$ μm) to the spectral data points, excluding obvious spectral features (e.g., the continuum). As a next step, we normalize our spectra to the fitted continuum as $F_{\nu,\mathrm{norm}} = 1 + (F_{\nu,\mathrm{obs}} - F_{\nu,\mathrm{cont}})/\langle F_{\nu,\mathrm{cont}} \rangle$, where $F_{\nu,\mathrm{obs}}$ is the observed *Spitzer* flux, $F_{\nu,\mathrm{cont}}$ is the fitted continuum, and $\langle F_{\nu,\mathrm{cont}} \rangle$ is the mean continuum value over the fitted wavelength interval. This normalization allows us to directly compare the different spectra and ensures that the shape of the spectral features remains identical to that in the original, unnormalized spectra.

To characterize the 10 μm amorphous silicate band, we determined the fluxes at different wavelengths across the silicate feature in the normalized spectra. The results of this analysis are

presented in § 3. Amorphous silicates also show a band at around 18 μm. However, this band blends with the (often rising) continuum emission, as can for instance be seen in Figure 1. This makes it difficult, if not impossible, to determine the band strength and position with sufficient accuracy for a meaningful analysis. We therefore opted not to use this band in our analysis. At longer (>20 μm) wavelengths, the emission features are mainly produced by crystalline silicates. To measure the observed band positions and strengths, we simultaneously fitted a Gaussian to each of the main spectral features in the normalized spectra. The results of this analysis are also presented in § 3. For the crystalline silicate emission bands in the 10 μm wavelength region, a slightly modified analysis method has to be applied. In this wavelength range, the emission bands overlap with, and can be dominated by, emission from small amorphous silicate grains. Also, polycyclic aromatic hydrocarbon (PAH) molecules may contribute to the observed emission in the short-wavelength range, overlapping with the emission features of the crystalline silicates. Therefore, the crystalline contribution can only be estimated by fitting a detailed grain model (discussed in the next section) that determines the contribution of the amorphous silicates and PAH molecules. After subtracting the fitted contribution of the amorphous silicates and PAH molecules, we applied an analysis for estimating the different crystalline silicate band strengths in the 10 μm wavelength region, similar to that used for the longer wavelength crystalline bands.

2.3. *Dust Models*

The grain model and analysis method for determining the physical properties of the dust grains contributing to the observed emission are similar to those successfully applied in previous studies of the 10 μm region (see Bouwman et al. 2001; van Boekel et al. 2005 for further discussion). Here, we also apply this method to the silicate emission at longer (~20–30 μm) wavelengths. Dust in protoplanetary disks most likely has a structure of highly irregular aggregates containing many different dust constituents, like the interplanetary dust particles collected in the Earth's upper atmosphere. Calculating the optical properties of such a complex structure has proven to be extremely difficult (e.g., Henning & Stognienko 1996). However, assuming that the aggregates are extremely porous, the individual constituents making up the aggregate may interact with the radiation field as separate entities, as is the case with IDPs (Molster et al. 2003). Therefore, we assume that the observed emission can be represented by the sum of the emission of individual dust species. Table 2 summarizes the dust species used in our analysis, including all dust species commonly identified in protoplanetary disks (e.g., Bouwman et al. 2001; van Boekel et al. 2005; Sargent et al. 2006).

Crystalline silicates such as forsterite (Mg_2SiO_4) and enstatite ($MgSiO_3$) have many strong and narrow resonances in the wavelength range covered by the IRS spectrograph. These rotational/ vibrational bands of the crystalline dust species allow for a much more accurate determination of chemical composition, grain size, and shape/porosity than is possible with the amorphous silicates. We find, as in the above-mentioned studies, that the pure magnesium end members of the olivine and pyroxene families give the best match to the observed spectral features. Based on the comparison between the band positions and strengths observed in our spectra and laboratory measurements (Fabian et al. 2001; Koike et al. 2003), we find no evidence for iron containing crystalline silicates. Still, a few open questions remain. Enstatite comes in the form of clino- and ortho-enstatite, each of which has a different crystalline structure. However, both forms show very similar emission bands at around 10 μm, making it hard to distinguish
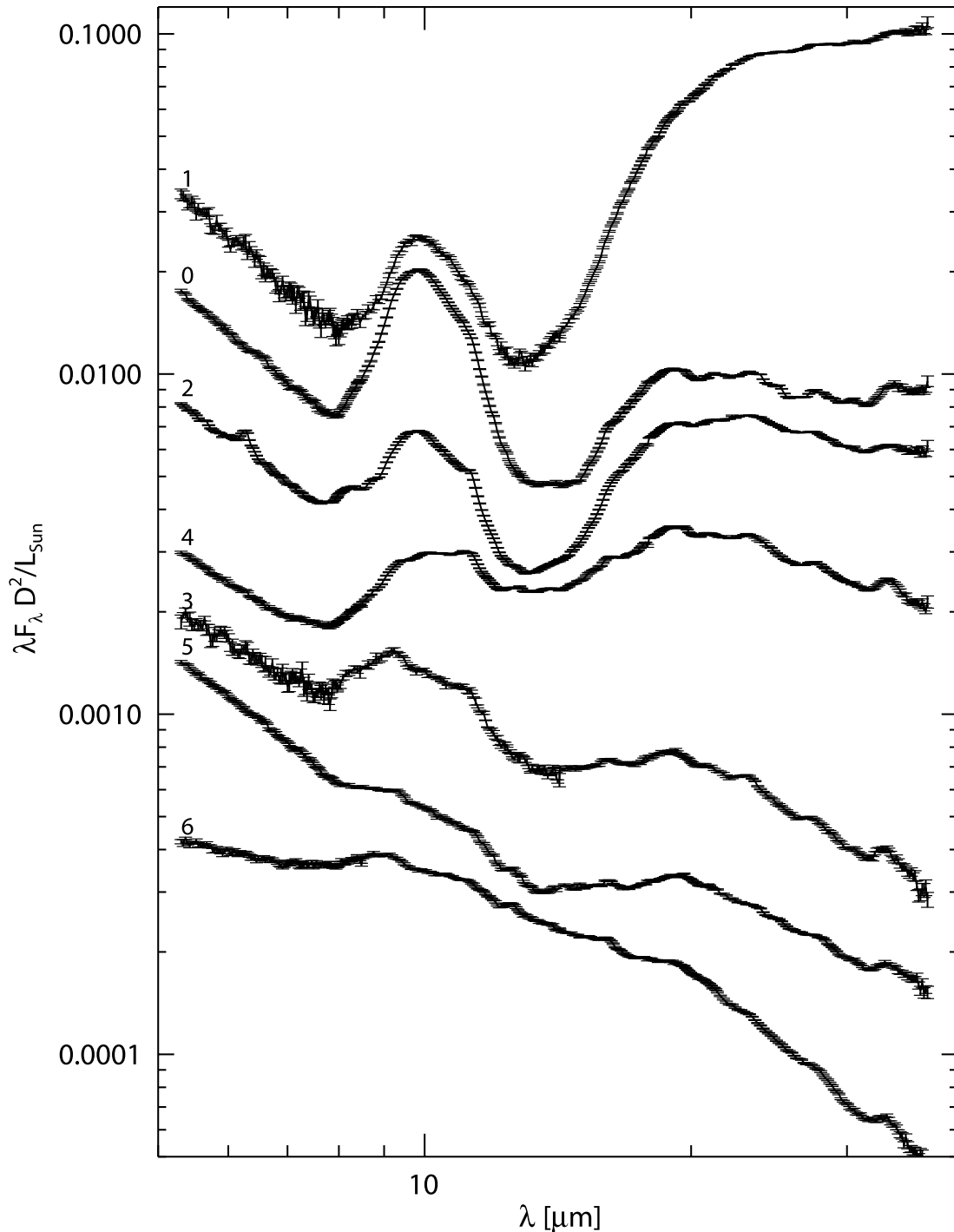
FIG. 1.—Spectral energy distributions of the TTS systems observed within the FEPS legacy program. Shown are the *Spitzer* low-resolution spectra scaled to the adopted distance and luminosity of the individual stars as listed in Table 1. For clarity, the spectra are offset from each other and ordered from top to bottom based on the observed slope of the SED by multiplying by 20, 5, 0.75, 1, 2.2, 0.25, and 0.2, respectively.

between them (e.g., Jäger et al. 1998; Koike et al. 2000). Only at the longer wavelengths can a clear difference between the emission properties be observed. Unfortunately, as we will discuss in the next chapter, no clear enstatite bands can be observed at the longer wavelengths, making it difficult to determine the exact enstatite structure. We therefore have chosen to use clino-enstatite, allowing for a direct comparison between our results and the study by van Boekel et al. (2005) of a sample of Herbig Ae-Be stars. A similar problem occurs for silica dust grains. Silica has nine polymorphs, among which are quartz, tridimite, and cristobalite, that

differ in crystal structure. While quartz is the most common form of these silicates found on Earth, the common form found in IDPs is tridimite (Rietmeijer 1988), and this is most likely also the most common form in protoplanetary disks. To our knowledge, no similar-quality laboratory measurements of tridimite exist that would enable us to perform an analysis identical to those performed for the other dust species. However, if one compares the amorphous form of silica and quartz, we observe similar bands. It might well be, as in the case of enstatite, that it will be difficult to tell the different forms of silica apart. As quartz is unlikely to exist in
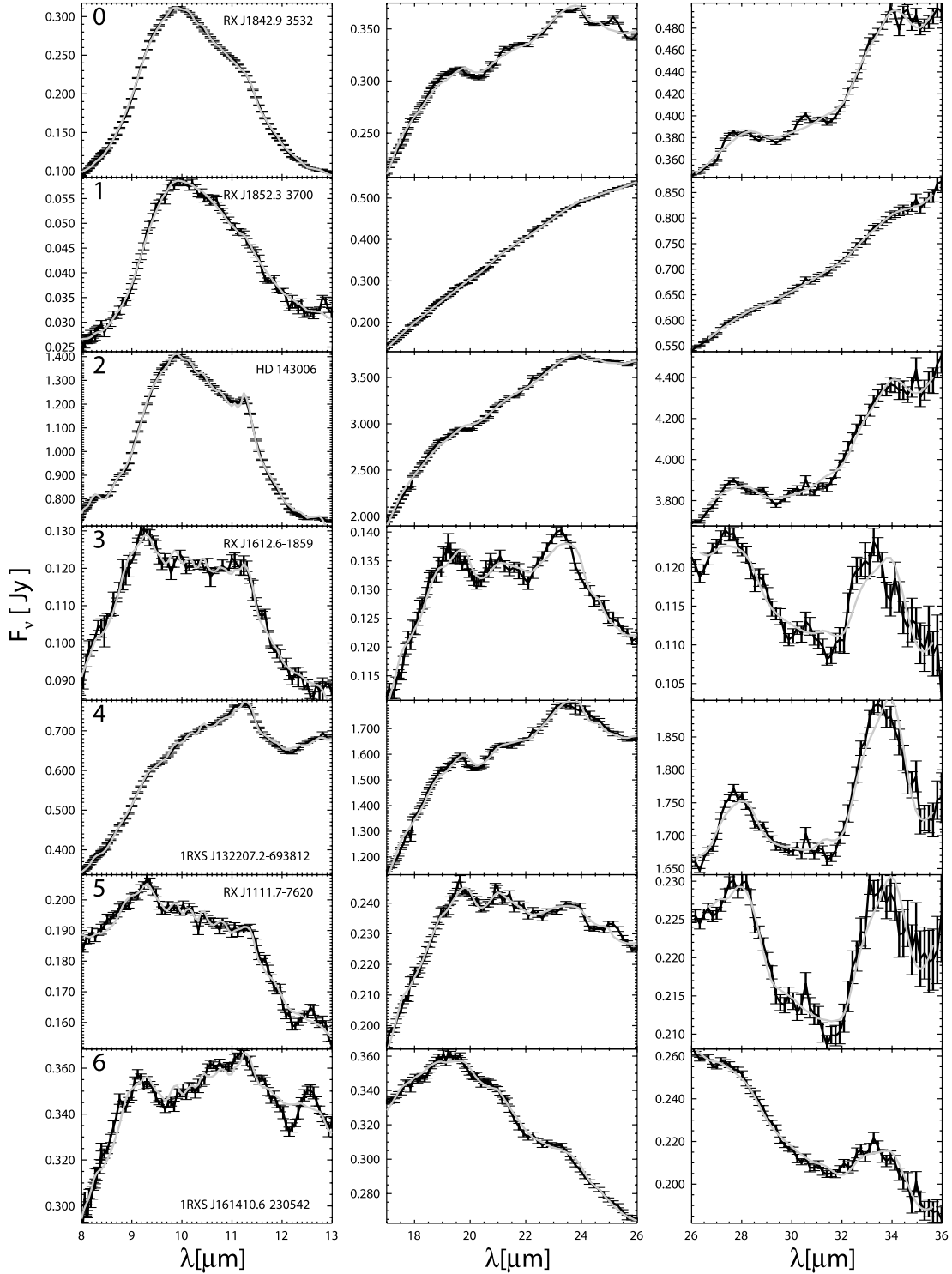
Fig. 2.—*Spitzer* low-resolution spectra of seven TTSs observed within the FEPS legacy program. The left panels show the spectra in the wavelength region between 8 and 13 μm, the central panels the spectral region between 17 and 26 μm, and the right panels the spectral region between 26 and 36 μm. The spectra are ordered from top to bottom according to the decreasing strength above continuum of the 10 μm silicate band. Also plotted in this figure is a compositional fit to the spectra (*light gray lines*). For details on the model fits, see § 2.3.

protoplanetary disks, we have opted to use an amorphous silicate with the stoichiometry of silica.

As has already been noted in previous studies (e.g., Bouwman et al. 2001), the observed emission bands of forsterite, enstatite, and silica cannot be reproduced assuming simple homogeneous spherical grains; rather, one has to adopt an inhomogeneous grain structure and/or nonspherical grain shape. Here, we use a distribu-

tion of hollow spheres (DHS; Min et al. 2005), which gives an excellent match to the observed band positions and shapes. DHS has an advantage over the widely used continuous distribution of ellipsoids (CDE; Bohren & Huffman 1983) in that it is also defined outside of the Rayleigh limit, making it possible to investigate the effects of grain size on the emission properties of the grains. One should realize that the above-discussed grain models, whether

ID	Species	State	Chemical Formula	Shape	Reference
1...........................	Amorphous silicate (Olivine stoichiometry)	A	$MgFeSiO_4$	Homogeneous	1
2...........................	Amorphous silicate (Pyroxene stoichiometry)	A	$MgFeSi_2O_6$	Homogeneous	1
3...........................	Forsterite	C	Mg_2SiO_4	Inhomogeneous	2
4...........................	Clino Enstatite	C	$MgSiO_3$	Inhomogeneous	3
5...........................	Silica	A	SiO_2	Inhomogeneous	4

NOTES.— For each component we specify its lattice structure, chemical composition, shape, and reference to the laboratory measurements of the optical constants. For the homogeneous spheres, we used Mie theory to calculate the opacities. For the inhomogeneous spheres, we used the distribution of hollow spheres (DHS; Min et al. 2005) to simulate grain deviating from perfect symmetry.
REFERENCES.— (1) Dorschner et al. 1995; (2) Servoin & Piriou 1973; (3) Jäger et al. 1998; (4) Henning & Mutschke 1997.

DHS or CDE, should not be taken as an exact representation of the structure/shape of a grain, but rather as a statistical description of the grain shape and structure and its deviation from sphericity and homogeneity (see Voshchinnikov et al. 2006; Min et al. 2006 for a further discussion of grain shape and porosity effects).

For the amorphous iron/magnesium silicates, the exact composition and grain shape cannot be constrained as well as it can be for the crystalline silicates. Models of the broad amorphous silicate resonances at ∼10 and ∼18 μm are to some extent degenerate. Silicate models with varying magnesium-to-iron ratios and different grain shapes/homogeneity can reproduce the observed bands (e.g., Min et al. 2007). To allow for a direct comparison with previous studies, we assume here that the amorphous silicates have an equal magnesium-to-iron atomic ratio and stoichiometries consistent with olivine and pyroxene. Furthermore, for the amorphous iron-magnesium silicates, we assume homogeneous, spherical grains for which we calculate the absorption coefficients using the Mie theory (e.g., Bohren & Huffman 1983) and the optical constants listed in Table 2.

To take into account the effect of grain size, we calculated for each of the different grain species the opacities for three volume-equivalent grain radii of 0.1, 1.5, and 6.0 μm. These grain sizes sample the range of spectroscopically identifiable grain sizes at infrared wavelengths at the S/N of our data. The resulting calculated opacities for three successive wavelength regimes are shown in Figures 3a, 3b, and 3c. We present our analysis of the various dust species in §§ 3.1, 3.2, and 3.3.

Apart from the silicate dust species, PAH molecules also contribute to the observed emission bands within the spectral range of the IRS instrument. These large molecules are not in thermal equilibrium with the radiation field, but are stochastically heated. Although many of the observed spectral features can be linked to specific vibrational modes and ionization states of the molecules, their exact compositions remain unclear. As our main focus in this paper is the solid-state component in the protoplanetary disks, we opted to use a template spectrum, based on observed profiles by Peeters et al. (2002) and van Diedenhoven et al. (2004), for estimating the contribution of PAH molecules to the spectra. We present this analysis in § 3.4.

The thermal infrared emission from protoplanetary disks is determined by the complex spatial distribution of individual dust species and their radial and vertical optical depth and temperature distributions. A completely self-consistent model of protoplanetary disks, such as a full radiative transfer calculation, would also have to account for processes such as radial and vertical mixing of circumstellar material and chemical and structural alteration of the dust grains under varying physical conditions in different parts of the disk. Furthermore, to uniquely constrain such models, spatially resolved observations as a function of wavelength (e.g., Thamm et al. 1994) are necessary. Instead, we employ a more simplistic approach that has been demonstrated to successfully reproduce the silicate emission features of HAeBe and TTS systems. Detailed self-consistent models (e.g., Men'shchikov & Henning 1997; Chiang & Goldreich 1997; Dullemond et al. 2001) have shown that the emission features originate from a warm optically thin disk surface layer on top of an optically thick disk interior, producing continuum emission. The basic assumption of our simple model is that the disk emission features can be reproduced by a sum of emissivities at a given temperature T_{dust}, and the continuum emission by the emission of a black body at a given temperature T_{cont}, which can be interpreted as the typical color temperature of the underlying continuum at a given wavelength.

We thus fit the following emission model using a linear least-squares minimization to the *Spitzer* low-resolution spectra:

$$F_\nu = B_\nu(T_{cont})C_0 + B_\nu(T_{dust})\left(\sum_{i=1}^{3}\sum_{j=1}^{5} C_{i,j}\kappa_\nu^{i,j}\right) + C_{PAH}I_\nu^{PAH},$$

$$(1)$$

where $B_\nu(T_{cont})$ denotes the Planck function at the characteristic continuum temperature T_{cont}, $B_\nu(T_{dust})$ is the Planck function at the characteristic silicate grain temperature T_{dust}, $\kappa_\nu^{i,j}$ is the mass absorption coefficient for silicate species j (five in total) and grain size i (three in total), I_ν^{PAH} is the PAH template emission spectrum, and C_0, $C_{i,j}$, and C_{PAH} are the weighting factors of the continuum, the silicate components, and the PAH contribution, respectively. For the single-temperature approximation to be meaningful, the width of the spectral region, and thus the temperature range, needs to be sufficiently narrow. Therefore, we have split the observed spectra into three bands: from 6 to 13 μm, from 17 to 26 μm, and from 26 to 36 μm. Apart from the previous considerations, these wavelength boundaries also ensure that both continuum and spectral features can be well characterized, and that multiple bands of the main crystalline silicates can be modeled simultaneously. This latter point is important, as it reduces the degeneracy problem of the overlapping emission bands of the different dust species. We have limited the maximum temperature in our fits to 1500 K, above which all silicate dust is expected to be vaporized.

Figure 2 shows the resulting best-fit models for the three spectral regions. As one can see, a good agreement between model and observations can be obtained using the dust species discussed in this section, without the need for additional components. The
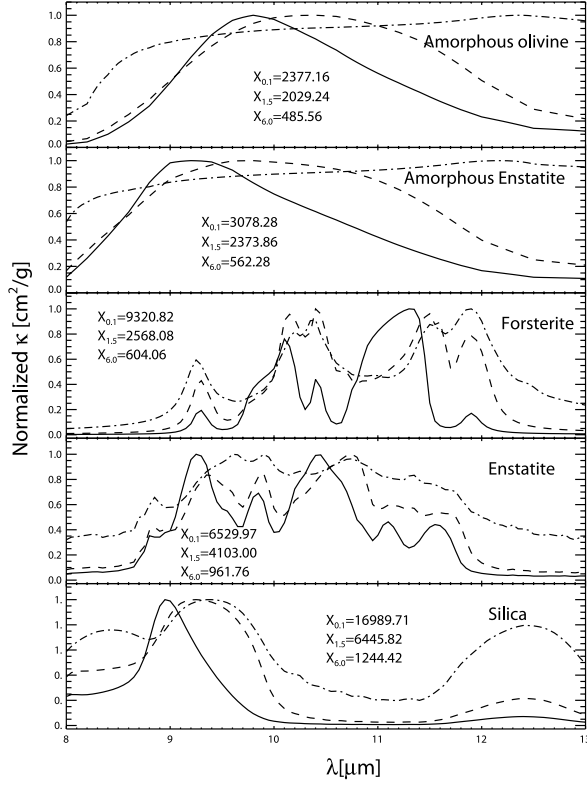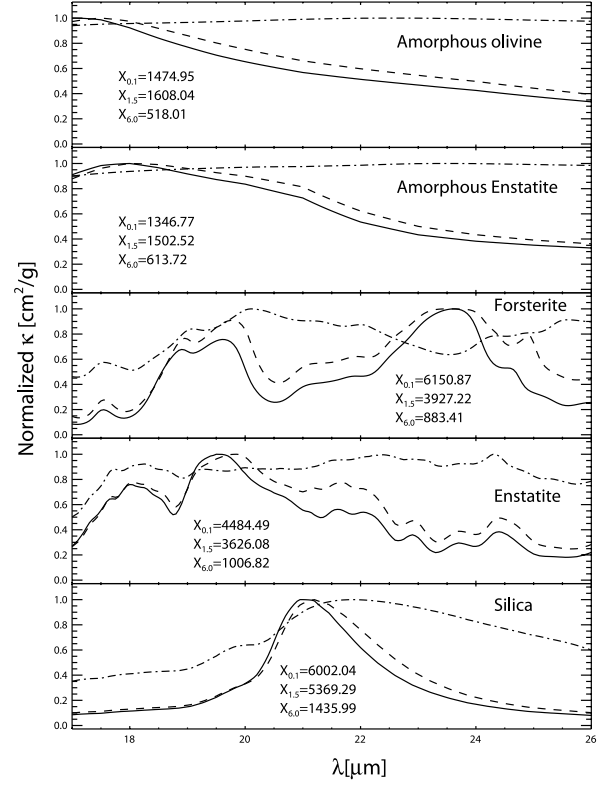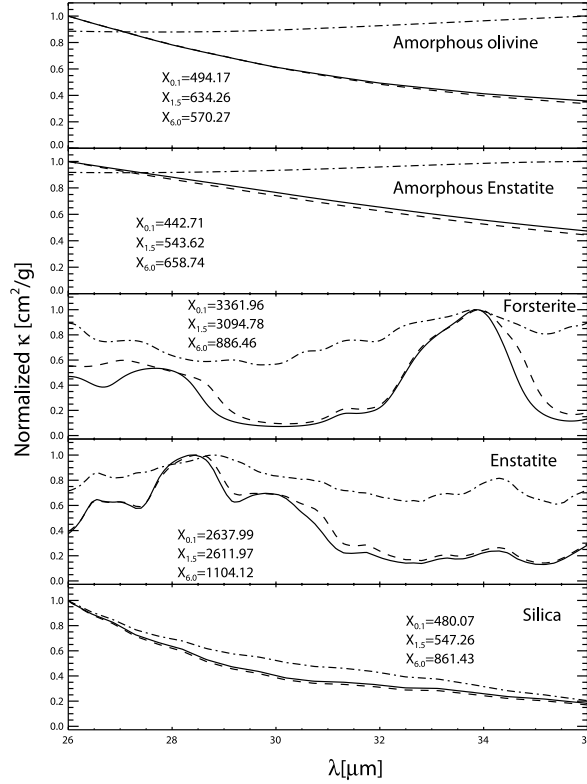
Normalized κ [cm²/g]

Amorphous olivine
$X_{0.1}=2377.16$
$X_{1.5}=2029.24$
$X_{6.0}=485.56$

Amorphous Enstatite
$X_{0.1}=3078.28$
$X_{1.5}=2373.86$
$X_{6.0}=562.28$

Forsterite
$X_{0.1}=9320.82$
$X_{1.5}=2568.08$
$X_{6.0}=604.06$

Enstatite
$X_{0.1}=6529.97$
$X_{1.5}=4103.00$
$X_{6.0}=961.76$

Silica
$X_{0.1}=16989.71$
$X_{1.5}=6445.82$
$X_{6.0}=1244.42$

λ[μm]

Fig. 3a

Amorphous olivine
$X_{0.1}=1474.95$
$X_{1.5}=1608.04$
$X_{6.0}=518.01$

Amorphous Enstatite
$X_{0.1}=1346.77$
$X_{1.5}=1502.52$
$X_{6.0}=613.72$

Forsterite
$X_{0.1}=6150.87$
$X_{1.5}=3927.22$
$X_{6.0}=883.41$

Enstatite
$X_{0.1}=4484.49$
$X_{1.5}=3626.08$
$X_{6.0}=1006.82$

Silica
$X_{0.1}=6002.04$
$X_{1.5}=5369.29$
$X_{6.0}=1435.99$

λ[μm]

Fig. 3b

Normalized κ [cm²/g]

Amorphous olivine
$X_{0.1}=494.17$
$X_{1.5}=634.26$
$X_{6.0}=570.27$

Amorphous Enstatite
$X_{0.1}=442.71$
$X_{1.5}=543.62$
$X_{6.0}=658.74$

Forsterite
$X_{0.1}=3361.96$
$X_{1.5}=3094.78$
$X_{6.0}=886.46$

Enstatite
$X_{0.1}=2637.99$
$X_{1.5}=2611.97$
$X_{6.0}=1104.12$

Silica
$X_{0.1}=480.07$
$X_{1.5}=547.26$
$X_{6.0}=861.43$

λ[μm]

Fig. 3c

Fig. 3.—Opacities scaled to unity for the different dust species listed in Table 2. Panels *a*, *b*, and *c* show the opacities between 8 and 13 μm, between 17 and 26 μm, and between 26 and 36 μm, respectively. In each panel, the solid lines, dashed lines, and dot-dashed lines represent the opacities for grain sizes of 0.1, 1.5, and 6 μm, respectively. Also indicated in each panel are the scaling factors for each of the opacity curves used in the normalization to unity.

resulting model parameters are listed in Table 3. We estimated the uncertainties in the derived band strengths and positions and the best-fit dust compositions by a Monte Carlo method as discussed in § 15.6 of Press et al. (1992). We generated a set of 100 spectra for each observation by randomly adding Gaussian noise with a 1 σ distribution equal to the error in the spectral extraction determined for each spectral data point. For each of these simulated spectra, we applied the analysis methods described above. Our quoted results represent the mean values of the derived quantities, and the error is the 1 σ standard deviation in the mean.

3. RESULTS

Following the dust modeling and spectral decomposition, our main science results are in the areas of dust coagulation from the analysis of the 10 μm amorphous silicate feature, dust settling from the additional analysis of the overall shape of the spectral energy distribution (SED), crystallinity from the analysis of the various silicate dust species, and PAHs, which remain in the residual emission after subtracting the identified silicates.

3.1. *Coagulation in Protoplanetary Disks*

Grain size strongly influences the infrared opacities, as can be seen in Figures 3a–3c. Typically, for the observations presented here, grain sizes (assuming compact grains) of up to 10 μm can be inferred spectroscopically. This is 2 orders of magnitude larger than the grain sizes typically derived for dust grains in the ISM (≤ 0.1 μm). For larger grains, the spectral signatures become too weak to distinguish them from continuum emission. Amorphous iron-magnesium silicates, which make up the bulk of the solid-state material in the ISM, show two broad spectral features at about 10 and 18 μm from which grain sizes can, in principle, be determined. The latter band, however, often blends with continuum emission from the disk interior and colder dust grains at larger radii, making it difficult to determine the grain size. For this reason, the 10 μm silicate band gives the most accurate information concerning amorphous silicate grain sizes. Many previous studies have shown that both the shape (Bouwman et al. 2001) and strength (van Boekel et al. 2003, 2005; Przygodda et al. 2003; Schegerer et al. 2006; Kessler-Silacci et al. 2005, 2006) of the 10 μm silicate features observed in HAeBe and TTS systems are mainly determined by the size of the amorphous silicate grains.

Figure 4 shows the correlation between the shape and strength of the 10 μm silicate feature as measured by the relation between the peak-over-continuum strength of the 10 μm silicate feature and the ratio of normalized fluxes at 11.3–9.8 μm (*filled symbols*) and at 8.6–9.8 μm (*open symbols*). We performed a Kendall's τ test on the data plotted in Figure 4. This test computes the probability that (x, y) pairs of data are correlated in the sense of the relative rank ordering of the x-values compared to the relative rank ordering of the y-values (Press et al. 1992). A value of Kendall's τ was computed along with the two-sided probability that the variables are not correlated ($\tau = -1$ indicates a perfect anticorrelation, while $\tau = 1$ indicates a perfect positive correlation). For the filled points in Figure 4, Kendall's $\tau = -0.905$, with a probability $P < 0.004$ that the data are uncorrelated. For the open points in Figure 4, we find that $\tau = -0.810$, with a probability $P < 0.011$ that the data are uncorrelated. We interpret these trends as confirmation that the strengths and shapes of the silicate features are correlated. Although crystalline silicate emission bands will also influence the shape of the 10 μm silicate band, the correlations of

Figure 4 can be best explained by a change in the typical size of the emitting dust grains. The dashed line shows the expected correlation for an amorphous silicate of olivine stoichiometry, with a grain size changing continuously from 0.1 μm (lower right) to 2 μm (upper left). The only exception is the 8.6 over 9.8 μm ratio of RX J1612.6−1859A (source number 3), where the ratio is dominated by an unusually strong emission from enstatite and silica.

Figure 5 shows the relation between the mass-weighted grain size of the amorphous iron-magnesium silicates (*open symbols*; right axis) as derived from our spectral decomposition of 0.1, 1.5, and 6 μm grains, and the peak-over-continuum value of the 10 μm silicate band. Examining this relation in more detail, we find a Kendall's τ of −0.81 for the rank ordering of peak-over-continuum emission compared to the mean size of amorphous silicate grains based on the analysis presented in Table 3. The probability of these variables not being correlated is 0.011. This correlation demonstrates that the peak-over-continuum ratio is correlated with the estimated size of the emitting amorphous iron-magnesium silicate grains. As a note of caution, recall that the exact values for the grain sizes derived are linked to the grain model used in the spectral decomposition. For reasons discussed in § 2.3, we use homogeneous spheres to model the amorphous silicates. More complex grain structures, such as fractal high-porosity grains, give qualitatively similar results (e.g., Voshchinnikov et al. 2006; Min et al. 2006), but require much larger aggregates to reproduce the observed band strengths.

3.2. *Coagulation and Dust Settling*

Having explored grain growth for our sample of T Tauri disks compared to the ISM grain population, we now ask what effect coagulation could have on the disk structure itself. As we do not have spatially resolved observations, we use the shape of the SED to infer the geometry of the disks. It has long been known that disk geometry strongly influences the shape of an SED (e.g., Kenyon & Hartmann 1987). Strongly flaring disks, which intercept a substantial fraction of the radiation from the central star at large radii, show a rising SED peaking at around 100 μm. "Flattened" disks, on the other hand, intercept far less of the radiation from the central star, and show a power-law-like SED decreasing with wavelength. Meeus et al. (2001) showed that the disks in HAeBe systems can be divided into two groups based on the shape of their SEDs. They interpret this bimodal behavior of the SED in terms of a bimodal disk geometry, which has either a flaring or a flattened disk structure. Recent spatially resolved observations seem to confirm the interpretation that different SEDs can be linked to different disk geometries (e.g., Leinert et al. 2004). As an explanation for the different disk geometries, two different models have been proposed: (1) grain growth and gravitational settling toward the disk midplane, and (2) "self-shadowing" of the disk surface at larger radii by the inner (∼0.1 AU) disk.

Coagulation models show that if the dust grains in the upper layers of a flared disk become sufficiently large, they will gravitationally settle toward the midplane of the disk, resulting in a flattened disk geometry (e.g., Schräpler & Henning 2004; Nomura & Nakagawa 2006). Recent model calculations concerning the effect of grain coagulation and settling on the SED show that the changing dust geometry from a flaring toward a flattened geometry due to the grain-settling results in SEDs is consistent with observations (D'Alessio et al. 2006; Dullemond & Dominik 2004b; Furlan et al. 2005, 2006).

As an alternative, Dullemond & Dominik (2004a) explain the variation in observed SED shapes for HAeBe and TTS systems

TABLE 3
BEST-FIT VALUES OF THE PARAMETERS IN OUR COMPOSITIONAL FITS TO THE 8–13 μm SPECTRAL REGION

ID	χ^2	T_c (K)	T_{dust} (K)	CONTINUUM FLUX CONTRIBUTION	AMORPHOUS OLIVINE Mass	AMORPHOUS OLIVINE $\langle a \rangle$	AMORPHOUS PYROXENE Mass	AMORPHOUS PYROXENE $\langle a \rangle$	FORSTERITE Mass	FORSTERITE $\langle a \rangle$	ENSTATITE Mass	ENSTATITE $\langle a \rangle$	SILICA Mass	SILICA $\langle a \rangle$	PAH CONTRIBUTION
							8–13 μm Spectral Region								
0	11.1 ± 0.5	$1500.0^{+0.0}_{-0.0}$	$324.6^{+6.9}_{-5.6}$	$0.5214^{+0.0009}_{-0.0009}$	$0.7902^{+0.0063}_{-0.0063}$	$1.16^{+0.09}_{-0.07}$	$0.1787^{+0.0071}_{-0.0072}$	$1.12^{+0.09}_{-0.08}$	$0.0146^{+0.0004}_{-0.0004}$	$0.1^{+0.0}_{-0.0}$	$0.0165^{+0.0016}_{-0.0015}$	$1.20^{+0.08}_{-0.09}$	...	...	$0.0066^{+0.0004}_{-0.0004}$
1	3.4 ± 0.3	$1500.0^{+0.0}_{-0.0}$	$257.4^{+3.9}_{-5.6}$	$0.6361^{+0.0027}_{-0.0025}$	$0.9872^{+0.0042}_{-0.0042}$	$3.08^{+0.07}_{-0.13}$	$0.0016^{+0.0064}_{-0.0014}$	$0.1^{+0.0}_{-0.0}$	$0.0016^{+0.0011}_{-0.0009}$	$0.1^{+0.0}_{-0.0}$	$0.0091^{+0.0036}_{-0.0038}$	$1.41^{+0.08}_{-0.32}$	$0.0006^{+0.0030}_{-0.0006}$	$1.5^{+0.0}_{-0.0}$	$0.0082^{+0.0015}_{-0.0017}$
2	17.2 ± 0.7	$1459.0^{+17.1}_{-13.5}$	$296.2^{+5.3}_{-6.2}$	$0.6255^{+0.0011}_{-0.0011}$	$0.4225^{+0.0120}_{-0.0058}$	$0.13^{+0.47}_{-0.03}$	$0.5296^{+0.0047}_{-0.0053}$	$5.30^{+0.06}_{-0.05}$	$0.0149^{+0.0003}_{-0.0003}$	$0.1^{+0.0}_{-0.0}$	$0.0330^{+0.0010}_{-0.0011}$	$1.496^{+0.004}_{-0.004}$	...	...	$0.0246^{+0.0003}_{-0.0003}$
3	8.8 ± 0.7	$1030.6^{+77.5}_{-94.7}$	$369.9^{+66.4}_{-44.0}$	$0.6792^{+0.0263}_{-0.0210}$	$0.2933^{+0.2511}_{-0.2375}$	$6.00^{+0.0}_{-0.09}$	$0.6452^{+0.2366}_{-0.2529}$	$4.85^{+0.34}_{-1.94}$	$0.0141^{+0.0044}_{-0.0018}$	$0.15^{+0.24}_{-0.04}$	$0.0342^{+0.0061}_{-0.0054}$	$1.13^{+0.13}_{-0.13}$	$0.0133^{+0.0040}_{-0.0027}$	$0.37^{+0.27}_{-0.22}$	$0.0103^{+0.0031}_{-0.0021}$
4	11.1 ± 0.5	$778.8^{+2.7}_{-14.6}$	$183.8^{+1.2}_{-14.8}$	$0.6054^{+0.0031}_{-0.0011}$	$0.6369^{+0.0367}_{-0.0412}$	$5.57^{+0.08}_{-0.05}$	$0.3279^{+0.0404}_{-0.0370}$	$2.27^{+0.45}_{-0.75}$	$0.0114^{+0.0003}_{-0.0005}$	$0.1^{+0.0}_{-0.0}$	$0.0238^{+0.0013}_{-0.0026}$	$0.97^{+0.04}_{-0.07}$	...	...	$0.0126^{+0.0007}_{-0.0004}$
5	4.0 ± 0.4	$1500.0^{+0.0}_{-0.0}$	$236.6^{+6.5}_{-7.2}$	$0.8544^{+0.0011}_{-0.0010}$	$0.8236^{+0.0138}_{-0.0160}$	$6.0^{+0.0}_{-0.0}$	$0.1060^{+0.0153}_{-0.0133}$	$0.1^{+0.0}_{-0.0}$	$0.0272^{+0.0025}_{-0.0023}$	$0.97^{+0.05}_{-0.06}$	$0.0349^{+0.0023}_{-0.0022}$	$1.39^{+0.07}_{-0.08}$	$0.0083^{+0.0019}_{-0.0015}$	$0.35^{+0.27}_{-0.21}$	$0.0022^{+0.0005}_{-0.0005}$
6	6.9 ± 0.4	$617.0^{+13.2}_{-7.1}$	$305.1^{+5.6}_{-5.8}$	$0.8206^{+0.0055}_{-0.0096}$	$0.5862^{+0.0810}_{-0.1153}$	$6.0^{+0.0}_{-0.0}$	$0.3728^{+0.1200}_{-0.0802}$	$5.999^{+0.001}_{-0.016}$	$0.0058^{+0.0005}_{-0.0005}$	$0.1^{+0.0}_{-0.0}$	$0.0249^{+0.0022}_{-0.0024}$	$1.21^{+0.08}_{-0.09}$	$0.0104^{+0.0009}_{-0.0009}$	$0.1^{+0.0}_{-0.0}$	$0.0066^{+0.0008}_{-0.0011}$
							17–26 μm Spectral Region								
0	28.3 ± 1.4	$46.3^{+3.8}_{-1.4}$	$118.0^{+0.0}_{-0.0}$	$0.0321^{+0.0022}_{-0.0018}$	$0.9592^{+0.0066}_{-0.0071}$	$1.5^{+0.0}_{-0.0}$	$0.0161^{+0.0073}_{-0.0069}$	$0.80^{+0.67}_{-0.67}$	$0.0192^{+0.0009}_{-0.0005}$	$0.14^{+0.11}_{-0.04}$	...	...	$0.0055^{+0.0005}_{-0.0005}$	$1.5^{+0.0}_{-0.0}$	...
1	7.0 ± 0.7	$105.3^{+30.1}_{-0.6}$	$84.95^{+0.05}_{-0.3}$	$0.2529^{+0.0186}_{-0.0289}$	$0.8650^{+0.0136}_{-0.0119}$	$1.61^{+0.14}_{-0.09}$	$0.1141^{+0.0122}_{-0.0136}$	$1.5^{+0.0}_{-0.0}$	$0.0099^{+0.0011}_{-0.0013}$	$0.72^{+0.21}_{-0.24}$	$0.0007^{+0.0015}_{-0.0006}$	$0.1^{+0.0}_{-0.0}$	$0.0104^{+0.0007}_{-0.0007}$	$1.5^{+0.0}_{-0.0}$	...
2	18.8 ± 1.0	$33.0^{+3.3}_{-3.3}$	$112.7^{+0.3}_{-0.3}$	$0.0096^{+0.0047}_{-0.0024}$	$0.7384^{+0.0195}_{-0.1520}$	$1.5^{+0.0}_{-0.0}$	$0.2459^{+0.0201}_{-0.1474}$	$5.84^{+0.10}_{-0.08}$	$0.0100^{+0.0005}_{-0.0004}$	$0.1^{+0.0}_{-0.0}$	...	...	$0.0057^{+0.0008}_{-0.0004}$	$1.5^{+0.0}_{-0.0}$	...
3	5.9 ± 0.6	$18.2^{+6.0}_{-3.2}$	$197.7^{+7.9}_{-6.4}$	$0.0013^{+0.0010}_{-0.0006}$	$0.1214^{+0.0348}_{-0.0353}$	$1.5^{+0.0}_{-0.0}$	$0.8628^{+0.0348}_{-0.0348}$	$5.67^{+0.04}_{-0.03}$	$0.0130^{+0.0007}_{-0.0007}$	$0.1^{+0.0}_{-0.0}$	$0.0001^{+0.0014}_{-0.0001}$	$0.1^{+0.0}_{-0.0}$	$0.0029^{+0.0008}_{-0.0008}$	$0.71^{+0.71}_{-0.55}$	...
4	13.0 ± 0.8	$106.0^{+5.4}_{-7.4}$	$152.6^{+2.6}_{-3.9}$	$0.1748^{+0.0513}_{-0.0388}$	$0.3846^{+0.0912}_{-0.0594}$	$1.5^{+0.0}_{-0.0}$	$0.5881^{+0.0614}_{-0.0967}$	$4.99^{+0.18}_{-0.39}$	$0.0226^{+0.0039}_{-0.0023}$	$0.1^{+0.0}_{-0.0}$	$0.0001^{+0.0001}_{-0.0001}$	$0.1^{+0.0}_{-0.0}$	$0.0047^{+0.0010}_{-0.0009}$	$1.13^{+0.34}_{-0.68}$	...
5	5.3 ± 0.5	$177.0^{+3.9}_{-2.6}$	$294.5^{+34.6}_{-31.3}$	$0.7317^{+0.0120}_{-0.0104}$	$0.0328^{+0.0784}_{-0.0311}$	$6.0^{+0.0}_{-0.0}$	$0.8255^{+0.0368}_{-0.0717}$	$1.5^{+0.0}_{-0.0}$	$0.0996^{+0.0090}_{-0.0071}$	$1.26^{+0.10}_{-0.10}$	$0.0206^{+0.0088}_{-0.0077}$	$0.1^{+0.0}_{-0.0}$	$0.0215^{+0.0052}_{-0.0051}$	$0.15^{+0.05}_{-0.56}$	...
6	3.9 ± 0.5	$340.0^{+9.7}_{-110.6}$	$155.1^{+71.6}_{-13.1}$	$0.6692^{+0.0308}_{-0.1003}$	...	...	$0.9643^{+0.0059}_{-0.0255}$	$1.43^{+0.85}_{-0.83}$	$0.0321^{+0.0157}_{-0.0051}$	$0.52^{+0.23}_{-0.29}$	$0.0025^{+0.0040}_{-0.0021}$	$0.1^{+0.0}_{-0.0}$	$0.0012^{+0.0106}_{-0.0011}$	$0.1^{+0.0}_{-0.0}$	...
							26.5–35.5 μm Spectral Region								
0	15.3 ± 2.0	$25.7^{+4.9}_{-5.3}$	$96.7^{+5.2}_{-5.3}$	$0.0726^{+0.0282}_{-0.0282}$	$0.0458^{+0.1059}_{-0.0396}$	$2.95^{+2.75}_{-2.51}$	$0.9341^{+0.0392}_{-0.1195}$	$0.66^{+0.65}_{-0.45}$	$0.0165^{+0.0012}_{-0.0009}$	$0.74^{+0.29}_{-0.30}$	$0.0036^{+0.0016}_{-0.0014}$	$1.08^{+0.41}_{-0.78}$	...	...	...
1	3.1 ± 0.6	$31.2^{+4.9}_{-13.9}$	$89.3^{+12.2}_{-12.2}$	$0.0515^{+0.0356}_{-0.0306}$	$0.5475^{+0.3181}_{-0.3382}$	$3.47^{+2.39}_{-2.11}$	$0.4425^{+0.3891}_{-0.2567}$	$1.78^{+3.33}_{-1.19}$	$0.0054^{+0.0028}_{-0.0013}$	$0.82^{+0.63}_{-0.52}$	$0.0011^{+0.0009}_{-0.0009}$	$0.48^{+1.01}_{-0.38}$	$0.0035^{+0.0331}_{-0.0045}$	$0.89^{+0.63}_{-0.83}$	...
2	6.0 ± 1.0	$33.6^{+16.2}_{-10.8}$	$134.0^{+21.5}_{-6.8}$	$0.1070^{+0.1931}_{-0.0649}$	$0.2973^{+0.1866}_{-0.2574}$	$5.16^{+0.81}_{-3.46}$	$0.6921^{+0.2567}_{-0.1864}$	$0.47^{+1.79}_{-0.35}$	$0.0101^{+0.0017}_{-0.0009}$	$0.47^{+0.42}_{-0.31}$	$0.0003^{+0.0012}_{-0.0003}$	$0.1^{+0.0}_{-0.0}$	$0.0002^{+0.0045}_{-0.0002}$	$0.1^{+0.0}_{-0.0}$	...
3	5.2 ± 0.8	$26.9^{+147.2}_{-16.9}$	$173.8^{+343.9}_{-37.5}$	$0.0980^{+0.0921}_{-0.0921}$	$0.1832^{+0.2281}_{-0.1675}$	$4.90^{+1.07}_{-4.52}$	$0.7364^{+0.2133}_{-0.3726}$	$1.10^{+4.52}_{-0.97}$	$0.0708^{+0.5710}_{-0.0529}$	$0.55^{+0.42}_{-0.31}$	$0.0061^{+0.0638}_{-0.0061}$	$0.1^{+0.0}_{-0.0}$	...	...	...
4	6.8 ± 0.9	$21.0^{+6.2}_{-5.3}$	$104.4^{+1.9}_{-4.5}$	$0.0259^{+0.0163}_{-0.0108}$	$0.0866^{+0.0621}_{-0.0577}$	$4.37^{+1.45}_{-2.80}$	$0.8956^{+0.0581}_{-0.0619}$	$0.28^{+0.51}_{-0.18}$	$0.0154^{+0.0010}_{-0.0008}$	$0.32^{+0.21}_{-0.17}$	...	...	$0.0024^{+0.0089}_{-0.0023}$	$0.1^{+0.0}_{-0.0}$	...
5	3.2 ± 0.6	$33.2^{+39.1}_{-16.6}$	$186.2^{+142.1}_{-33.5}$	$0.1327^{+0.3108}_{-0.1136}$	$0.0230^{+0.1883}_{-0.0213}$	$2.27^{+3.91}_{-1.28}$	$0.9521^{+0.1950}_{-0.1950}$	$2.39^{+3.91}_{-1.95}$	$0.0165^{+0.0043}_{-0.0023}$	$0.38^{+0.37}_{-0.25}$	$0.0079^{+0.0049}_{-0.0032}$	$0.82^{+0.60}_{-0.61}$	$0.0005^{+0.0053}_{-0.0005}$	$0.1^{+0.0}_{-0.0}$	...
6	4.2 ± 0.6	$15.85^{+5.8}_{-5.5}$	$174.5^{+121.1}_{-19.7}$	$0.0266^{+0.3374}_{-0.0193}$	$0.0448^{+0.1745}_{-0.0443}$	$5.67^{+0.34}_{-5.89}$	$0.9216^{+0.0524}_{-0.1567}$	$1.09^{+0.60}_{-0.89}$	$0.0193^{+0.0060}_{-0.0022}$	$0.76^{+0.28}_{-0.32}$	$0.0137^{+0.1975}_{-0.0101}$	$0.1^{+0.0}_{-0.0}$	...	...	...

NOTES.—The abundances of the various dust species are given as a percentage of the total dust mass, *excluding* the dust responsible for the continuum emission. Also listed is the mass-averaged grain size of the different dust species. If a species was not found or was unconstrained by the spectra, this is indicated by ellipses. The PAH and continuum flux contributions are listed as percentages of the total integrated flux over the 10 μm region contained in these components. These are measures for the relative flux contributions, but cannot be interpreted as relative dust masses. The resulting best-fit model spectra are plotted in Fig. 2 (*light gray lines*).
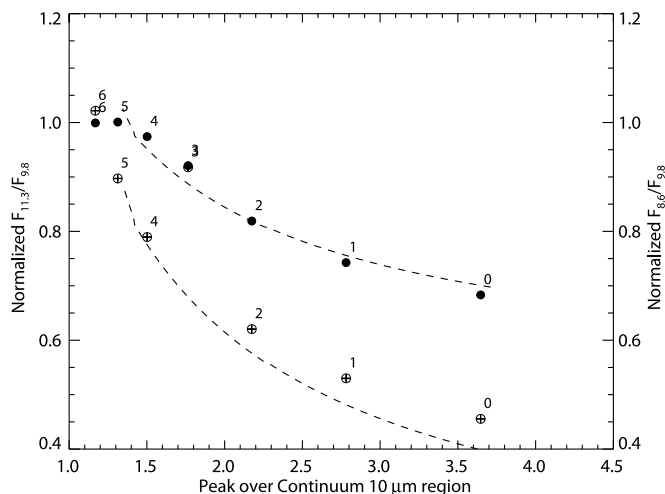
FIG. 4.—Correlations between the strength and the shape of the 10 μm silicate band. The filled circles show the correlation between the peak-over-continuum ratio of the 10 μm silicate band and the ratio of the normalized flux at 11.3 μm over 9.8 μm (left axis). The open circles show the correlation between the peak-over-continuum ratio and the ratio of the normalized flux at 8.6 μm over 9.8 μm (right axis). Note that the formal error on the plotted quantities is smaller than the size of the circles. The numbers correspond to the ID numbers of our target stars as listed in Table 1. Also plotted in this figure (dashed lines) is the calculated behavior for both flux ratios of amorphous olivine grains for a continuously changing grain size from 0.1 μm (lower right) to 2.0 μm (upper left).

as differences in disk heating caused by differences in the self-shadowing of the disk surface. If the central star cannot directly irradiate the outer disk surface due to a puffed-up inner disk (which causes the surface of the outer disk to lie in the shadow of the inner disk), the temperature, and thus the scale height, of the shadowed region will be substantially lower than that of a disk with a directly irradiated surface. This lower temperature will result in a smaller pressure scale height of the disk and thus in a flattened geometry.

A way to test these models is to look for a relation between the measured grain sizes and the geometry of the disk. In Figure 6, we explore the relation between the amorphous silicate grain sizes as measured by the strength of the 10 μm silicate feature, and the
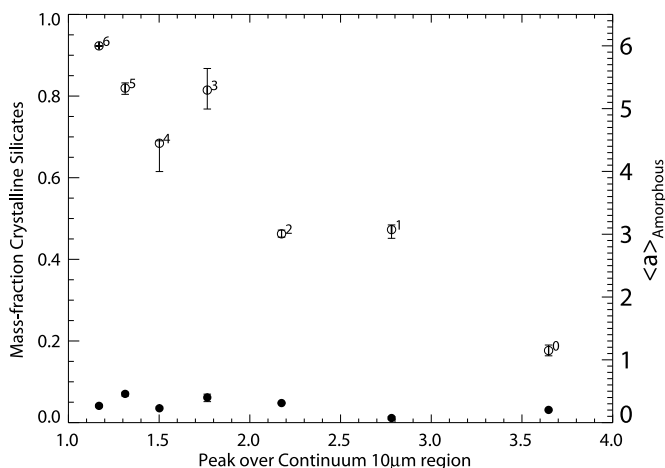

FIG. 5.—Correlation between the derived mass fraction of crystalline silicates (filled circles; left axis) and (1) the peak-over-continuum ratio of the 10 μm silicate band and (2) the mass-averaged grain size of the amorphous silicates (open circles; right axis) emitting in this wavelength region. As the amorphous grains become bigger, the 10 μm silicate band becomes weaker. No correlation between the mass fraction of crystalline silicates and the typical grain size of the amorphous silicates can be observed.
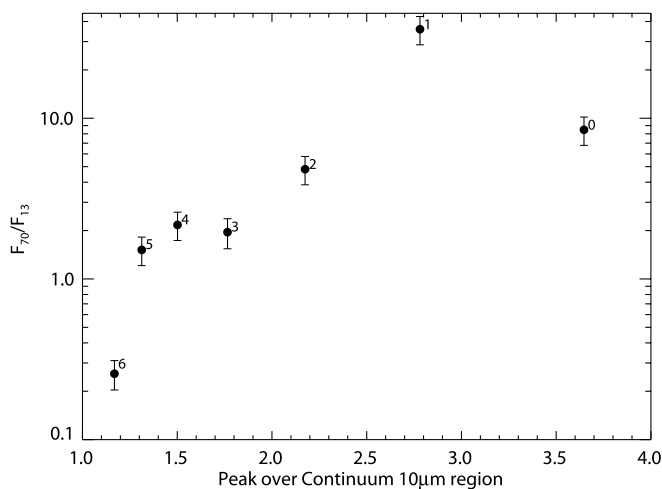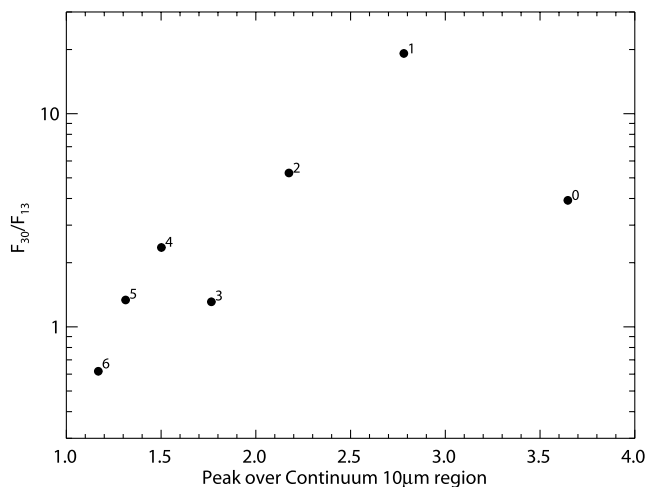

FIG. 6.—Correlation between the far-IR slope of the spectral energy distribution, a measure of disk geometry, and the peak-over-continuum ratio of the 10 μm silicate band, a measure of the typical grain size. The far-IR slope is measured by the ratio of the flux at 30 μm over 13 μm (top) and at 70 μm over 13 μm (bottom). A clear correlation can be seen. As the 10 μm silicate band becomes weaker, the slope of the spectral energy distribution decreases. The 13 and 33 μm fluxes are synthetic photometry points derived from the Spitzer low-resolution spectra, and the 70 μm fluxes are photometric data from the MIPS instrument on board the Spitzer Space Telescope. Note that the error bars in the upper panel are the same size as the symbols and reflect the small internal uncertainties in our IRS spectra. The larger error bars in the lower panel mainly reflect the uncertainties in the absolute flux calibration between the MIPS and IRS instruments.

disk flaring angle as measured by the 30 μm over 13 μm (top) and the 70 μm over 13 μm (bottom) flux ratios. Here, the 13 and 30 μm fluxes are synthetic photometry points derived from our IRS spectra using 1 and 2 μm wide boxes, respectively, that are centered on the quoted wavelengths. The 70 μm fluxes are derived from observations by the Multiband Imaging Photometer for Spitzer (MIPS). Figure 6 provides quantitative evidence that these variables are indeed correlated. The Kendall's τ for the top panel is 0.7 with $P = 0.03$, while for the bottom panel $\tau = 0.81$ with $P = 0.01$, both of which indicate a significant positive correlation. As we saw in Figure 5, the peak-over-continuum ratio of the 10 μm silicate features is strongly anticorrelated with grain size. As a result, we conclude from Figure 6 that grain size is strongly correlated with SED slope. Larger flaring angles of the disk produce larger flux ratios because of enhanced emission from cooler grains farther out in the disk that are exposed to the stellar flux by the flaring. With increasing grain size (decreasing 10 μm
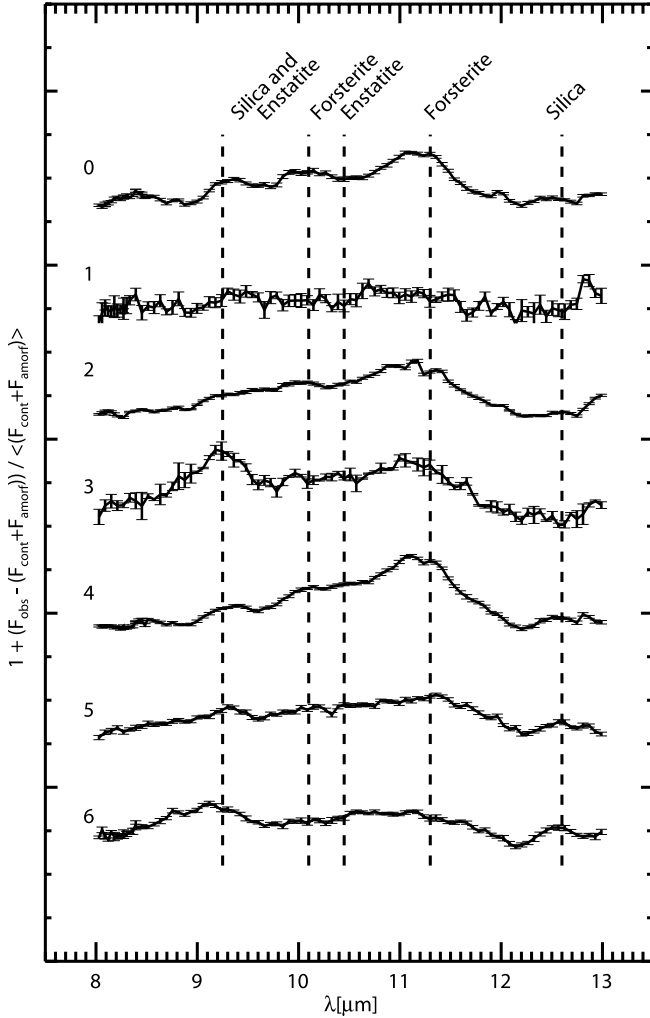
FIG. 7.—Emission bands of crystalline silicates in the 10 μm spectral window. Shown are the *Spitzer* low-resolution spectra normalized to the fitted amorphous silicate, PAH, and continuum model (see also § 2.3). The normalized spectra all have the same vertical scale between 0.97 and 1.15 but are offset for clarity. The spectra are ordered from top to bottom by decreasing 10 μm silicate band strength. The ID numbers correspond to those listed in Table 1. Also indicated in this figure are the positions of the main emission bands of silica, forsterite, and enstatite dust grains.

FIG. 8.—Continuum-normalized spectra of the FEPS TTS sample. Shown are the *Spitzer* low-resolution spectra between 17 and 36 μm normalized to the fitted continuum using a low-order polynomial (see also § 2.3). The normalized spectra all have the same vertical scale between 0.97 and 1.15 but are offset for clarity. The spectra are ordered from top to bottom by decreasing 10 μm silicate band strength. The ID numbers correspond to those listed in Table 1. Also indicated in this figure by the dashed and dotted lines are the positions of the main spectral features of forsterite and silica.

silicate band), the flaring angle of the disk appears to decrease (as traced by the slope of the SED toward longer wavelengths). Our results are in qualitative agreement with the model predictions of D'Alessio et al. (2006) and Dullemond & Dominik (2004b) and provide direct spectroscopic evidence for the link between the typical size of the dust grains and the disk structure. These results suggest that in TTS systems, it is coagulation and grain settling toward the midplane that determines the disk geometry, and thus the SED, rather then self-shadowing by the disk.

3.3. *Crystalline Silicates in Protoplanetary Disks*

The analysis of features produced by crystalline silicates provides important information on dust processing in protoplanetary disks. At present, no crystalline silicates have been observed in the diffuse ISM. Kemper et al. (2005) place an upper limit of 1% on the crystalline silicate mass fraction of the diffuse ISM. The much higher mass fractions observed in protoplanetary disks (e.g., Bouwman et al. 2001; van Boekel et al. 2005; ∼5% in this study) therefore imply that the observed crystalline silicates had to be formed in the disks themselves, rather then having been incor-
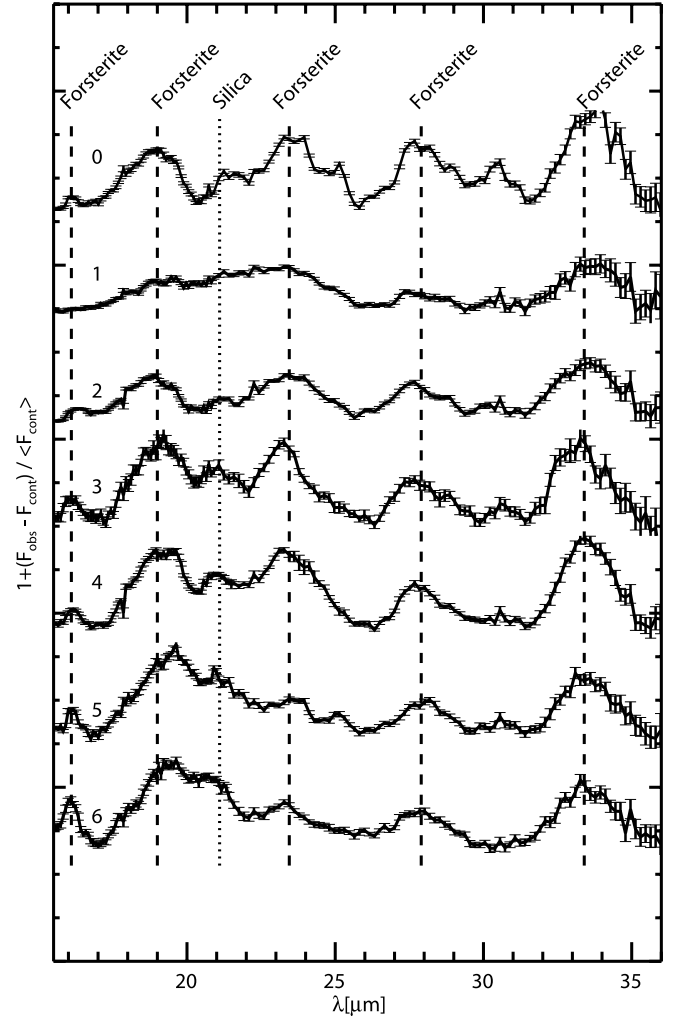
porated directly from the ISM into the disk (see Henning et al. 2005). This makes crystalline silicates a tracer of dust processing and evolution in protoplanetary disks. Figures 7 and 8 show the observed crystalline silicate bands at mid- and far-IR wavelengths, respectively, for our TTS sample. As described in § 2.2, the spectra have been normalized and, for the 10 μm regime, corrected for the amorphous silicate contribution. These normalized spectra clearly show the emission bands characteristic of emission from the crystalline dust species forsterite, enstatite, and silica. Using the opacities plotted in Figures 3a–3c, these three crystalline dust species, in combination with the amorphous silicates, produce an excellent fit to the *Spitzer* spectra as shown in Figure 2. The overall mass fraction of crystalline silicates based on the spectral decomposition of the 10 μm silicate band is around ∼5% (see also Table 3). We find no conclusive evidence for other crystalline silicates. Interestingly, other crystalline dust species, such as iron sulfides or oxides, can be expected to exist in protoplanetary disks (e.g., Pollack et al. 1996). Looking at Figures 2 and 8, weak features at 25.5 μm (source numbers 0 and 5) and 30.5 μm (source numbers 0 and 3) can be observed that are not properly
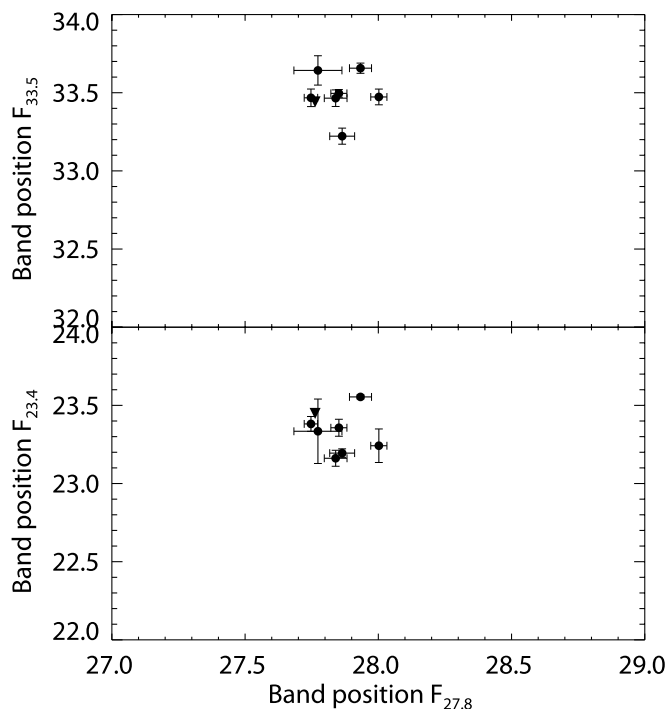
Fig. 9.—Comparison between the forsterite band position at 27.8 μm and that of the 33.5 μm feature (*top*) and the 23.4 μm feature (*bottom*). Also indicated are the calculated nominal band positions for 0.1 μm forsterite grains (*filled triangles*). [*See the electronic edition of the Journal for a color version of this figure.*]

Fig. 10.—Comparison between the measured strength of the forsterite bands at 11.3 μm (plotted on the *x*-axis) and 10.1 μm (*filled circles*), between the 33.5 μm (plotted on the *x*-axis) and the 27.8 μm spectral features (*open circles*), and between the 23.4 μm (plotted on the *x*-axis) and the 27.8 μm spectral features (*filled triangles*).

reproduced by our dust model. These features, however, are (1) not conclusively seen in the other targets, (2) have bands that do not coincide with known bands of materials like iron sulfide or iron oxide (Begemann et al. 1994; Henning et al. 1995), and (3) evince no clear relation between these weak bands. The possibility that these very weak bands are an instrumental artifact in the form of some residual fringing cannot be ruled out at this stage.

3.3.1. *Crystallinity and Grain Size*

As for amorphous dust grains, the shape, strength, and wavelength positions of the emission bands of the crystalline dust species yield information about the typical size of the emitting dust grains. As the crystalline silicates have many narrow spectral features that are sensitive to the shape, size, and composition of the dust grains, an excellent determination of the grain properties can be made. Using the analysis method described in § 2.2, Figures 9 and 10 show the correlations between the measured positions and strengths of the main forsterite resonances in our TTS sample. No trend in the band positions can be observed, which hardly vary from the nominal position expected for 0.1 μm sized grains (*filled triangles*). This is in sharp contrast to the results for the amorphous silicate component, where grain sizes of at least 6 μm are required to reproduce our observations. Also, the band ratios between the main forsterite resonances do not substantially vary from source to source. By comparing the strengths of neighboring bands, which minimizes the influence of possible source-to-source variations in the mass-over-temperature distribution, a linear relation can be observed. This relation reflects differences in the crystalline mass fractions in the different sources, rather than differences in the grain sizes of the crystalline silicates. A Kendall's τ test for the data plotted in Figure 10 results in $\tau = 0.81$ with $P = 0.011$ for the 11.3 μm versus 10.1 μm band strength, $\tau = 0.90$ with $P = 0.004$ for the 33.5 μm versus 27.8 μm band strength, and $\tau = 0.24$ with $P = 0.45$ for the 23.4 μm versus
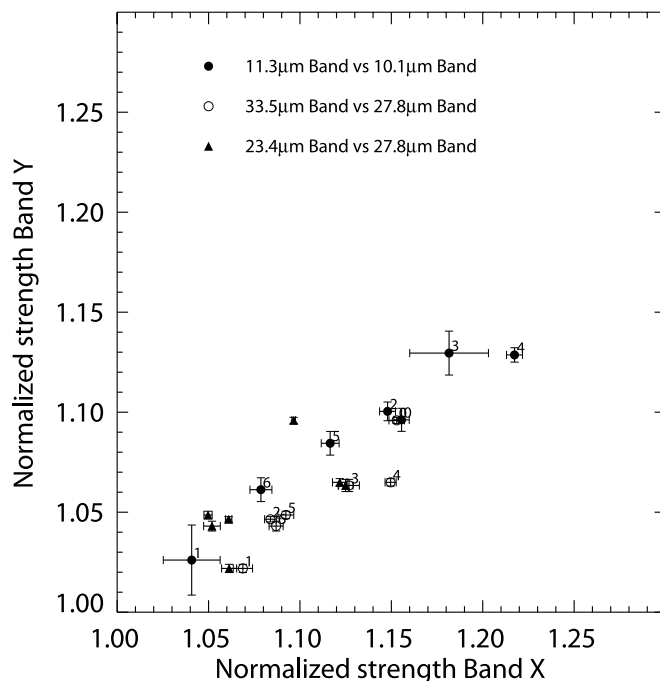
27.8 μm band strength. The apparent lack of correlation between the 23.4 and 27.8 μm band strength most likely reflects the difficulty in fitting an accurate local continuum underneath the 23.4 μm band. Still, those sources showing the strongest 23.4 μm bands also show the strongest bands at 27.8 μm.

From the spectral decomposition in the 10 μm wavelength region (see also Table 3), we determined the relative mass fraction of crystalline silicates contributing to the crystalline emission bands. Figure 5 also shows the relation between the observed amorphous silicate grain size and the crystalline silicate mass fraction. A Kendall's τ test gives $\tau = -0.43$ with $P = 0.18$, suggesting reasonable probability that the crystallinity and grain size of the (bulk) amorphous dust are uncorrelated. Determining the mass fraction of crystalline silicates depends on how well one can determine the mass fraction of the amorphous dust component. Within the 10 μm spectral region, probing the warmest dust, this poses no problem, as the amorphous silicates show a clear spectral signature. At the longer ($\sim$20 μm) wavelengths, which probe the colder dust at larger disk radii, amorphous silicates lack clear spectral signatures, which makes it difficult to determine the physical properties of the colder grains. However, the strengths of the emission bands over the local continuum in the $\sim$20–30 μm spectral region still provide a measure of the relative crystalline mass fraction as a function of wavelength, and thus as a function of temperature and of radial distance in the disk. Figure 11 compares the strength of the 10 μm silicate band (a measure of the typical grain size of the amorphous silicates) to the observed band strengths and positions of three of the main crystalline silicate bands. No conclusive correlation between the amorphous and crystalline bands can be observed, implying that neither the observed crystalline mass fraction nor the size of the crystals is correlated with the grain size of the amorphous dust, and thus that grain growth and crystallization appear to be unrelated. A Kendall's τ test for the relation between the peak-over-continuum value versus the strength and
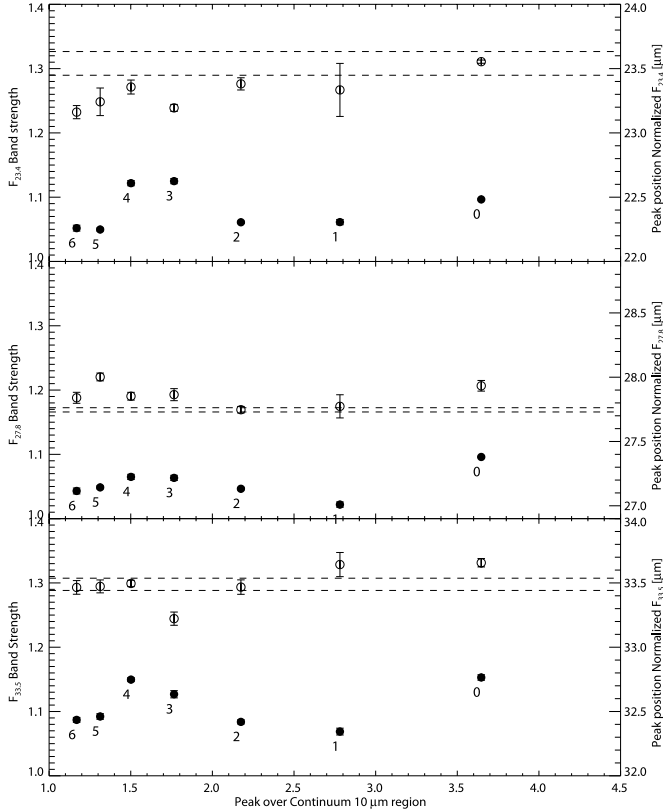
FIG. 11.—Correlations between the peak-over-continuum ratio of the 10 μm silicate band and the band strengths (*filled circles*; left axis) and positions (*open circles*; right axis) of three spectral emission bands of crystalline silicates. The top, middle, and bottom panels show the correlations for the 23.4, 27.8, and 33.5 μm bands, respectively. As one can see, both the position and the normalized band strength of these crystalline silicate bands show almost no variations and are not correlated to the silicate emission at 10 μm.

ishes. It is, therefore, crucial to have an accurate determination of the grain size of the (bulk) amorphous silicates. If we had used a smaller maximum grain size in our spectral decomposition, we would have estimated that no amorphous silicates are present in the 1RXS J161410.6−230542 system, leading to a 100% crystalline silicate mass fraction. This would, consequently, have led to a relation between the grain size of the amorphous dust and the crystallinity, as was noted by van Boekel et al. (2005). This result could be an artifact arising from an underestimation of the maximum grain size in their ground-based observations, leading to a lower mass estimate of the amorphous dust component. Compared with these ground-based studies, we should note that the *Spitzer* data have the advantage of allowing for a determination of the continuum outside the spectral window that is accessible from the ground. This results in a better characterization of the strength of the 10 μm silicate band, and thus of the grain size, especially in the case of very weak emission features.

3.3.2. The Crystallization Process

Apart from the comparison between the crystalline and the amorphous emission bands, the intercomparison between the crystalline spectral features can provide crucial information. Although we do not spatially resolve the protoplanetary disks, one can make an estimate of the size of the emitting region at a given wavelength from model calculations of the temperature distribution in the disk around a typical TTS (e.g., Kessler-Silacci et al. 2007). Kessler-Silacci et al. (2007) argue that the silicate feature at around 10 μm originates from the disk surface at around 1 AU from the central star. The spectral features observed at the longest wavelengths, at around 30 μm, correspond to a temperature of ∼120 K, the temperature at which a blackbody would emit most of its radiation at the given wavelength. Assuming a λ^{-1} dependency for the dust opacity and a typical stellar temperature and radius of 5500 K and 1 $R_{\odot}$, respectively, dust grains attain a temperature of 120 K at a radius of about 15 AU from the central star. This implies that with the IRS instrument we can probe the inner ∼15 AU of a disk in a TTS system. The dust composition of the disks beyond ∼15 AU cannot be determined, as the dust grains at these large radii are too cold to emit at wavelengths covered by the IRS spectrograph. Comparing the relative band strengths of forsterite in the 10 μm wavelength region, which probes the warmest dust, with the forsterite bands at longer wavelengths, which probes the colder dust component farther out in the protoplanetary disks, a possible trend can be observed (see Fig. 12). A Kendall's τ test for the relation between the 11.3 μm peak strength and the peak strengths of the 23.4, 27.8, and 33.5 μm bands results in $\tau = 0.52$ with $P = 0.1$, $\tau = 0.71$ with $P = 0.024$, and $\tau = 0.62$ with $P = 0.051$, respectively.

On average, those systems showing the strongest forsterite emission bands in the 10 μm spectral region also show the strongest bands at the longer wavelengths. One could interpret this possible correlation as evidence of a global crystallization process, where the crystallinity of the inner ∼15 AU of the disk is increased from nondetectable ISM values to the observed mass fractions of ∼5%, as measured in the 10 μm spectral region. Whether this means that the crystalline silicates are formed throughout the entire inner disk, or formed locally and then redistributed throughout the inner disk, will be discussed in § 4. One should note that due to the uncertainties in determining the amorphous mass fractions in a quantitative way at longer wavelengths (see also § 2.3), the radial density profile of the crystalline silicates remains uncertain. It is possible that in colder parts of the disk, at larger radial distances, the fraction of crystalline grains deviates from that determined for the inner parts. However, our
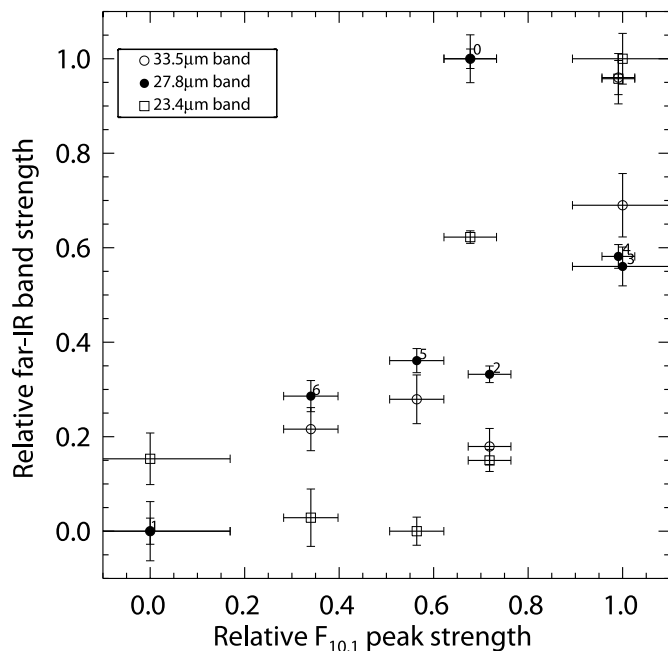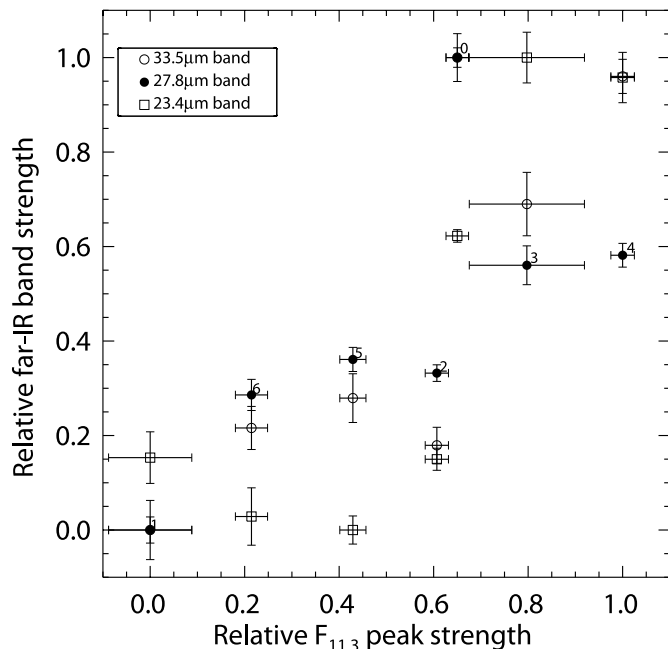
position of the 27.8 μm band results in $\tau = 0.147$ with $P = 0.65$ and $\tau = -0.048$ with $P = 0.88$, respectively. For the relation between the peak-over-continuum value versus the strength and position of the 33.5 μm band, we find $\tau = 0.048$ with $P = 0.89$ and $\tau = 0.52$ with $P = 0.1$, and for the relation between the peak-over-continuum value versus the strength and position of the 23.4 μm band, we find $\tau = 0.33$ with $P = 0.29$ and $\tau = 0.62$ with $P = 0.051$, respectively. As discussed in the previous paragraph for Figure 10, the possible weak correlation we observe for the 23.4 μm band is most likely due to a systematic problem in correctly determining the local continuum using a polynomial fit. As we can see in Figure 1, the shape of the SED in the 20 μm region varies considerably. As shown in § 3.2, there is a correlation between the shape of the SED and the peak-over-continuum value of the 10 μm silicate band. The possible correlation with the 23.4 μm band, therefore, might simply reflect a systematic difference in the local continuum estimate between sources with an SED that rises toward longer wavelengths and sources with a decreasing SED.

At first glance, the spectrum of a source such as 1RXS J161410.6−230542 (Fig. 2, *bottom left panel*) seems to exhibit a much higher crystalline mass fraction than a source such as RX J1842.9−3532 (Fig. 2, *top left panel*). The apparently more pronounced crystalline silicate bands in the former TTS system, however, do not reflect a larger crystalline mass fraction, but rather less amorphous silicate emission. As the amorphous grains grow with respect to the crystalline silicates, their relative opacities decrease, and hence their contribution to the observed spectra dimin-

FIG. 12.—Correlations between the measured band strengths of the crystalline silicate features in the 20–35 μm wavelength region and those observed in the 10 μm spectral region. The top figure shows the comparison between the band strength of the 11.3 μm and that of the 33.5 μm spectral feature (*open circles*), the 27.8 μm band (*filled circles*), and the 23.4 μm band (*open squares*). The lower figure shows a similar comparison but with the band strength of the 10.1 μm spectral feature.

FIG. 13.—Correlation between the enstatite mass fraction of the crystalline silicates as measured in the 10 μm spectral window and the enstatite mass fraction of the crystalline silicates derived from analyzing the longer wavelength features between 20 and 35 μm.

suggests that both crystalline species are to a certain extent unrelated, and a general increase of forsterite abundance seems not to correspond to a similar increase in enstatite abundance. Although the crystalline silicate mass relative to that of the amorphous silicates cannot be determined at the longer wavelengths, our spectral decomposition as a function of wavelength, and thus of the radius of the emitting regions, can determine the mass ratios between the different crystalline silicates. In Figure 13, we plot the relation between the enstatite fraction of the crystalline grain populations as measured within the 10 μm wavelength region and that determined from the longer wavelength spectral regions. Surprisingly, these results imply that the mass fraction of enstatite varies in the radial direction, with a larger enstatite fraction in the warmer inner disk than in the colder outer (~5–15 AU) regions. Another difference between the forsterite and enstatite grain population is the typical grain size. The grain size of the enstatite grains (~1 μm) is larger than that of the forsterite grains (~0.1 μm). Again, this points toward differences in the formation mechanism and/or conditions producing these crystalline species. The implications of the above results will be discussed in § 4.

3.4. PAH Emission in Protoplanetary Disks around T Tauri Stars

So far, little is known about the presence of PAH molecules in disks around low-mass pre-main-sequence stars. Systems with a relatively strong UV field can readily excite PAH molecules, as is observed for the more massive and luminous Herbig Ae-Be systems, where clear PAH emission signatures can be seen (e.g., Meeus et al. 2001; Sloan et al. 2005). Although observations of UV-poor reflection nebula and PAH laboratory measurements and models (Li & Draine 2002; Mattioda et al. 2005) show that longer wavelength photons can also excite PAH molecules, little evidence has been found for IR-emission bands from stochastically heated molecules or very small grains from the circumstellar disks around low-mass stars as studied in this paper. After carefully fitting our silicate model, a residual feature centered at 8.2 μm could be seen in the model-subtracted spectrum of five of the observed targets, which we tentatively identify with emission from stochastically heated PAH molecules. Figure 14 shows the

results show that, irrespective of the exact radial profile, the crystallinities of the innermost (~1 AU as measured at 10 μm) and outer (~5–15 AU as measured at wavelengths ~20–30 μm) disk regions are related.

A similar comparison for the enstatite emission bands is difficult, as our spectra show no features that can be uniquely identified with enstatite at the longer wavelengths. Comparing the strength of the main enstatite band at 9.2 μm and the longer wavelength bands of forsterite, we find no clear correlation. This
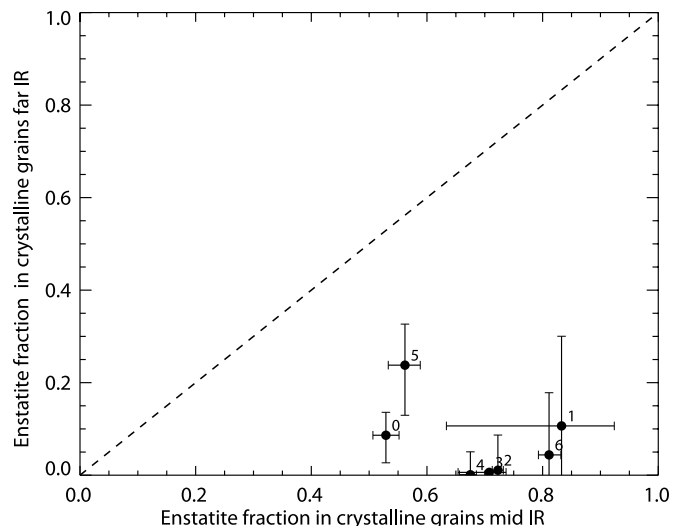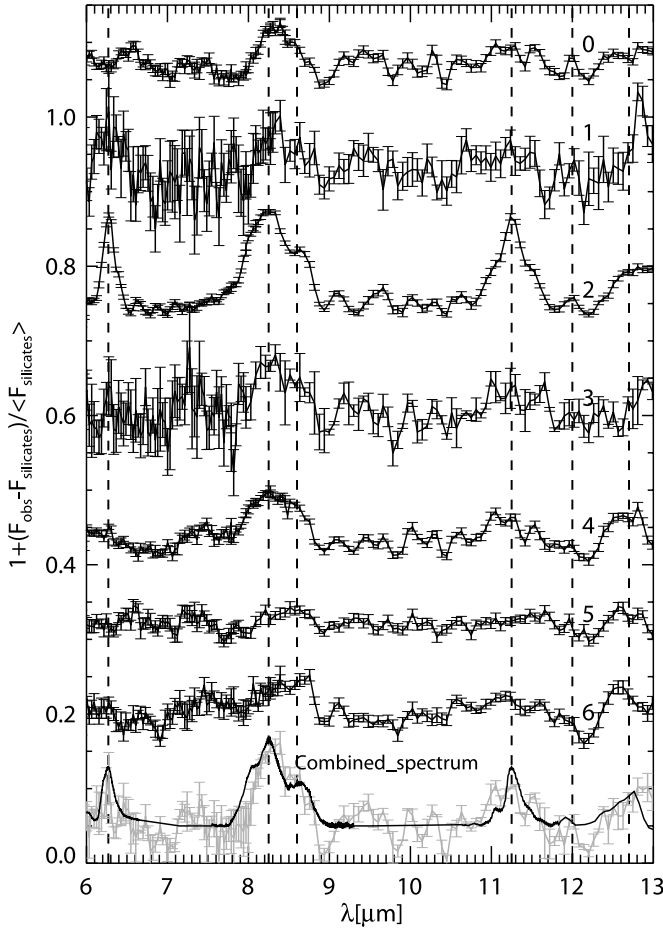
FIG. 14.—Observed PAH emission bands in the spectra of the FEPS TTS sample. Shown are the *Spitzer* low-resolution spectra normalized to the fitted silicate model (see also § 2.2 and Table 3). The first five spectra clearly show an emission feature at 8.2 μm, which we assign to emission from PAH molecules. Shown at the bottom of the figure is the average spectrum of source IDs 0, 1, 3, and 4, overplotted with the PAH template spectrum used in our fitting procedure. The dashed lines mark the positions of the main PAH bands. [*See the electronic edition of the Journal for a color version of this figure.*]

normalized residual spectrum after subtraction of the best-fit silicate model. The strongest bands can be seen in the residual spectrum of HD 143006 (source number 2), the most luminous source in our sample (G6/8 spectral type), which also shows clear evidence for emission bands at 6.2 and 11.2 μm.

As the PAH molecules require stellar photons to be excited, the molecules contributing to the emission bands have to be located at the optically thin surface layers of the disk, in direct view of the central star. As many papers have shown, for the Herbig Ae-Be systems (e.g., Meeus et al. 2001; Acke & van den Ancker 2004) there exists a direct correlation between the presence of PAH emission bands and the shape of the SED, which can be used as a measure of the flaring angle of the disk. Those disks having an SED consistent with a flattened disk structure, and hence a less illuminated disk surface, show little or no evidence of PAH emission. These results are also confirmed by spatially resolved spectroscopy showing that the PAH emission bands come from the flaring surface at larger radii of the disk (van Boekel et al. 2004a). We observe a similar trend, where those sources with SEDs consistent with more flattened disk structures show no clear evidence for the 8.2 μm feature. This apparent correlation between the lack of the 8.2 μm feature and the flaring angle of the disk, therefore, suggests that this emission band is not due to

an unidentified dust species in thermal equilibrium, but rather a stochastically heated large molecule or very small grain species at the disk surface.

Surprisingly, the observed band in the 8 μm region is not centered between 7.7 and 7.9 μm, where PAH emission is usually observed. The band position at 8.2 μm has only been measured in the spectra of a few other sources. Peeters et al. (2002) observed this band position in two post-AGB stars, and Sloan et al. (2005) observed the feature in the HAeBe system HD 135344. The observed bands in these three objects, however, show a slightly broader profile than is observed in the TTS systems. The observed relative weakness or absence of the 6.2 and 11.2 μm features with respect to the 8.2 μm band is consistent with the Peeters et al. (2002) and Sloan et al. (2005) studies. Furthermore, the HAeBe system from the latter study, which shows the 8.2 μm PAH band, has the lowest UV-flux of the four systems discussed in that paper, which would be consistent with our observations of lower luminosity systems. Presently, no conclusive explanation for the carrier of the 8.2 μm feature has been put forward. We can only speculate that the chemistry, ionization state, and/or structure should be substantially different for our sources compared to the PAH population in HAeBe systems. Li & Draine (2002) argue that in an environment low in UV, where longer wavelength photons excite the PAHs, the PAH molecules have to be ionized and/or large to be excited. The presumably much stronger X-ray emission in the TTS systems with respect to their higher mass counterparts may also play a role here, driving a different chemistry and ionization state. On the one hand, X-ray photons may increase the electron abundance in the gas, which would reduce the PAH ionization. On the other hand, a strong X-ray field could directly ionize the PAH molecules (multiple times) due to the Auger effect, and thereby change them or even destroy the smallest of them.

4. DISCUSSION

The circumstellar disks in T Tauri star systems are believed to be the sites of ongoing planet formation, and thus represent an analog for the protosolar nebula. As the disks evolve with time, the submicron-sized dust grains present at the formation time of the disks coagulate to form larger objects and eventually planet(esimal)s (Beckwith et al. 2000; Henning et al. 2006). By studying the characteristics and evolution of the disk and its dust composition, valuable insights can be obtained into the processes leading to the formation of planets, and important constraints on disk and planet formation models can be derived. Also, by analogy, TTS systems can provide clues into the early evolution of the solar system. In the following, we will discuss the implications of the findings presented in the previous sections. Note that our sample only spans a limited range in stellar parameters and consists of older, long-surviving disks. Our conclusions are applicable to similar systems, but possible effects of stellar properties or age on the evolution of circumstellar disks cannot be directly addressed by this study. For this, our results will have to be compared to the disk properties of a larger sample, spanning a wide range in stellar properties and evolutionary stages.

4.1. *Grain Growth and Disk Structure*

Based on our analysis of low-resolution infrared spectra of seven TTS systems obtained with the *Spitzer Space Telescope*, we find clear evidence of processing and growth of the silicate dust species present in their protoplanetary disks. We interpret observed variations in the thermal emission from amorphous silicate dust species as evidence for grain sizes that are substantially

different from those observed in the ISM, and argue for grain growth within the protoplanetary disks. For the first time, we find a clear correlation between the strength of the amorphous silicate feature, which measures the typical size of these grains, and the shape of the mid-infrared SED, which measures the disk scale height, i.e., the flaring of the disk. In the literature, two possible explanations have been put forward to explain the differences in disk flaring, the first of which is the self-shadowing of the disk due to an enhanced scale height of the innermost parts. Self-shadowing prevents the central star from illuminating the surface of the outer disk, which is required to sufficiently heat the disk and cause it to flare (Dullemond & Dominik 2004a). The second explanation argues for grain growth and the consequent gravitational settling toward the disk midplane (e.g., Schräpler & Henning 2004; Nomura & Nakagawa 2006; D'Alessio et al. 2006; Dullemond & Dominik 2004b; Furlan et al. 2005, 2006) as the causes of the differences in disk flaring. Our results, which link an increase in grain size to a decrease in the disk flaring, clearly argue for the latter explanation.

An earlier study by Apai et al. (2004), which studied the brown dwarf system CFHT-BD-Tau 4, also suggested a correlation between the strength of the silicate emission band and the shape of the SED. Acke & van den Ancker (2004) studied a sample of HAeBe systems observed with *ISO*. Because no correlation could be found between the observed silicate emission bands and the shape of the SED, the authors concluded that their observations were consistent with the self-shadowing disk model rather than with the coagulation and grain settling model. In an apparent contradiction, Acke et al. (2004) showed a correlation between grain size, as measured by the (sub)millimeter slope of the SED, and the disk flaring angle, which was based on the ratio of the near- to mid-IR excess. The latter results argue for coagulation and grain settling toward the midplane as the explanation for the observed bimodal distribution of SEDs, which is consistent with our findings here for lower mass solar-type stars.

We suspect that the correlation between the derived grain size and the disk flaring from IR spectroscopy has been missed so far for the HAeBe systems because of the stellar luminosity of A and B type stars, which is at least 1 order of magnitude higher than the later type stars studied here. Observations of HAeBe systems will, therefore, probe a much larger region of the circumstellar disk than the observations of TTS or brown dwarf systems for any given wavelength, by at least a factor 2–3. Given that coagulation and settling are functions of density and thus radius, gradients in the observed grain size and disk structure are to be expected. Probing a much larger region of the disk, therefore, could lead to the loss of any clear correlations In the HAeBe systems.

4.2. *The Formation of Crystalline Silicates*

All of the systems studied in this paper show emission from crystalline silicates, which constitutes further evidence for dust processing within the protoplanetary disks, since interstellar dust, the material present at the formation time of the disks, shows no evidence for crystalline silicates. The results of the spectral analysis of the crystalline silicate emission can be summarized as follows.

1. All observed targets show emission bands of crystalline silicates at both higher ($\sim$300–500 K) temperatures, probed in the 10 μm spectral window, and lower ($\sim$100 K) temperatures, probed in the 30 μm spectral region.

2. The observed emission bands are consistent with emission from the pure magnesium silicates forsterite and enstatite, and silica. No conclusive evidence for other species has been found.

3. The average grain size of the crystals is much smaller than that of the amorphous silicates. While amorphous silicates require grain sizes up to 6 μm, the crystalline emission is more consistent with a size of $\sim$0.1–1 μm.

4. We find no conclusive evidence for a correlation between the mass fraction of the crystalline silicates and the grain size of the amorphous silicates.

5. The average grain size of the enstatite grains as derived from the modeling of the 10 μm spectral region is systematically larger than that of the forsterite grains.

6. The strength of the forsterite emission features in the 10 μm wavelength region and those at the longer wavelengths seem to be correlated. This could be interpreted as evidence that the crystalline mass fraction is increased from ISM values to the observed mass fractions of about $\sim$5% throughout the entire inner $\sim$15 AU of the disk.

7. We find a change in the relative abundance of the different crystalline silicates between the innermost ($\sim$1 AU) warm dust population, which is dominated by enstatite, and the population at the colder, outer disk regions at larger radii ($\sim$5–15 AU), which are dominated by forsterite. This change in relative abundances points toward a radial dependence of either the formation mechanism of the crystalline silicates, or the (non)equilibrium conditions under which they formed, and also argues against substantial radial mixing of processed material from the inner to the outer parts of the disk (see paragraphs below for a detailed discussion).

How can we incorporate the above results for the crystalline silicates into a consistent picture of the physical processes occurring in a protoplanetary disk? As all of our targets show similar crystalline mass fractions and compositions, these physical processes can be expected to occur in all protoplanetary disks. The formation of forsterite and enstatite requires temperatures above $\sim$1000 K (e.g., Hallenbeck et al. 2000; Fabian et al. 2000). Such high temperatures are reached near the central star, where dust grains can be readily heated by the stellar radiation field. In an early active disk phase, the accretion energy can provide an additional heat source for the dust in the midplane regions of the inner disk (e.g., Bell et al. 2000). At these high temperatures, crystalline silicates can be formed either through annealing of the amorphous silicates (see Wooden et al. 2005 for an overview) or by gas-phase condensation/annealing and gas-solid reactions in a cooling gas (Davis & Richter 2004; Petaev & Wood 2005). Our observations show, however, that a substantial fraction of the crystalline silicates have temperatures ($\sim$100 K) far below the required crystallization temperature. This implies that either large-scale radial mixing is occurring, transporting the crystalline silicates from the hot inner parts to the cooler outer disk (e.g., Bockelée-Morvan et al. 2002), or that an additional localized and/or transient heating mechanism is operating in the cooler regions of the disk at larger radial distances from the central star. Such an additional heating mechanism might be provided by shock waves in which gas and dust grains are heated to the required temperatures of above 1000 K (Harker & Desch 2002; Desch et al. 2005).

The question now is whether our results can distinguish between different formation mechanisms and/or locations for the crystalline silicates. The presence of forsterite and enstatite, which are respectively the magnesium-rich end members of the olivine and pyroxene solid-solution series, combined with a lack of evidence for crystalline silicates containing substantial amounts of iron, suggests that they formed as high-temperature, gas-phase condensates (Davis & Richter 2004; Gail 2004). The presence of high-temperature condensates at lower temperatures indicates

that complete equilibrium condensation is not taking place in protoplanetary disks, since otherwise these species would have been transformed to other ferromagnesian silicates during cooling. Although the exact order in which the different dust species condense out from a cooling gas depends on the gas pressure and isolation of the condensed dust grains from the surrounding gas (Petaev & Wood 2005), most models predict forsterite to be condensed out first, followed by the formation of enstatite at slightly lower temperatures through solid-gas reactions between forsterite and SiO_2 gas. Iron will condense out slightly before or after forsterite as metallic iron grains rather than being incorporated into silicates. The slightly larger grain size of enstatite compared to forsterite can be the result from the gas-solid reactions and the broader temperature range (and thus a longer formation window in a slowly cooling gas) under which enstatite can be formed and is stable.

An alternative formation mechanism for forsterite and enstatite is the annealing of amorphous silicates without evaporating/recondensating the parent grain. The annealing process critically depends on the structure of the amorphous material and the oxygen partial pressure of the surrounding gas (i.e., reducing or oxidizing conditions). To prevent the formation of iron containing olivine and pyroxene minerals, the amorphous grains have to be annealed under reducing conditions. Davoisne et al. (2006) show that carbon combustion, which locks up the oxygen in the form of CO rather then in FeO, will cause the iron to precipitate as metallic particles and not be incorporated into a silicate. Thompson et al. (2002) showed that forsterite and silica, independent of the stoichiometry of the amorphous material, will always form, but that the formation of enstatite follows through solid-solid reactions between forsterite and silica. The effectiveness and speed of this reaction critically depend on the structure of the amorphous grains. In highly porous grains, such as those formed from smokes, the contact surfaces between the individual subunits will be small, and therefore reactions will be slow and will require substantial structural modification (such as melting) of the amorphous grain. For compact glassy amorphous silicates, the formation of enstatite can proceed immediately. As in the case of direct condensation, this secondary formation of enstatite through forsterite alteration could also explain why we observe a slightly larger grain size for enstatite than for forsterite.

Apart from the above considerations, two additional observational constraints can be imposed to distinguish between annealing and condensation as the main formation mechanism for crystalline silicates, namely summary points (3) and (4). The implication of these two observations is that the simultaneous presence of both large amorphous grains and small crystalline grains is *not* caused by a preferential transformation of small amorphous grains into crystalline silicates, leaving the larger amorphous grains. In other words, the observed change in grain size toward larger grains is caused by grain growth rather than the removal of the smaller amorphous grain population through crystallization in a distribution of grain sizes. If the latter had been the case, a correlation between amorphous grain size and crystalline mass fraction would have been observed. This, together with the fact that no large crystalline grains are observed, implies that either the crystals form as gas-phase condensates, that the large amorphous aggregates are disrupted before annealing, or that the main crystallization process occurred before coagulation.

Gas-phase condensation can naturally explain any difference in grain size between the amorphous and crystalline grains. In the case of an evaporation/condensation zone in the disk, where first the amorphous grains are evaporated, after which crystalline species can condense out if the gas cools, no relation between the original grain size distribution of the amorphous dust and that of the crystalline grains will exist. Annealing of large amorphous grains, on the other hand, will lead to the formation of large crystals. It is therefore necessary to disrupt the larger aggregates before they are annealed. A gradual heating of dust grains as they approach the hot inner disk is unlikely to fulfill this requirement. Annealing by shock waves could be a more plausible scenario, as it could also provide the mechanism to disrupt the larger amorphous aggregates. This formation mechanism would be similar to that of chondrules (e.g., Desch et al. 2005).

In the case of an early formation time of the crystalline silicates, that is, before coagulation and during the high-accretion phases, viscous dissipation can efficiently heat the disk up to several AU from the central star (e.g., Bell et al. 2000). An early formation time would imply that the crystalline silicate content of protoplanetary disks would remain fixed during their further evolution. This is consistent with previous studies, which reported no correlations between the processing of the silicates and systemic ages (e.g., van Boekel et al. 2005; Kessler-Silacci et al. 2006, 2005), although any correlation might also be lost due to the large uncertainties in age determinations. On the other hand, all systems studied in this paper show crystalline silicates. Studies of on average younger samples show that a substantial fraction of disks show no crystalline silicates (e.g., 50%; Kessler-Silacci et al. 2006). This would argue in favor of crystallinity increasing with time. Furthermore, recent studies of FU Orionis objects show no sign of crystalline silicates, independent of whether the silicate emission originates in disks or envelopes (Quanz et al. 2006, 2007; Green et al. 2006). If the notion is correct that the FU Orionis–type objects represent the early high-accretion stages of TTS evolution, crystalline silicates should be present if the bulk of the crystalline silicates were to form during the early evolution of the disks. Interestingly, Quanz et al. (2006) show that FU Orionis already shows signs of grain growth. If coagulation sets in this early, an alternative scenario for the formation of crystalline silicates is required.

Note that there is no difference in coagulation behavior between crystalline and amorphous silicates. The difference in grain size between the crystalline and amorphous silicates can be interpreted in terms of the optical properties of larger composite aggregates. Suppose a population of small, predominantly amorphous dust grains coagulates into larger aggregates. These larger aggregates will obviously consist mainly of amorphous material, but with a few crystalline grains that are isolated from each other and that will therefore interact with the radiation field as separate entities. The optical properties of such composite aggregates will likely resemble those of the combined properties of a larger amorphous grain with smaller crystalline particles, similar to what is observed in cometary spectra and IDPs.

The two remaining summary points to be discussed here, point (6) and most importantly point (7), place further constraints on the formation mechanism of the crystalline silicates and on the location in the disk where the crystalline silicates are forming. On the one hand, our data suggest a general increase in the crystalline mass fraction in the inner $\sim$15 AU of the disks; on the other hand, we observe a gradient in the crystalline dust composition within this inner region. The changing forsterite-over-enstatite mass ratio points to differences in the condensation or annealing conditions. As discussed in the previous paragraphs, the formation of enstatite follows after the formation of forsterite. The absence of enstatite or a much lower enstatite mass fraction derived from the longer wavelength bands, which probe the cooler dust at about 5–15 AU, compared to the mass ratio derived from the 10 μm wavelength region, shows that

much less or even none of the forsterite is converted into enstatite at larger radial distances from the central star. Consideration of gas-phase condensation as the formation mechanism for the crystalline silicates implies nonequilibrium condensation conditions at larger disk radii, unlike in the innermost disk regions. If forsterite forms locally at ∼5–15 AU in the disk, it has to be isolated from the surrounding SiO gas before they react to form enstatite. This could be achieved by coagulation or by rapid cooling of the surrounding gas, which both inhibit the gas-solid reactions leading to the formation of enstatite. Alternatively, if forsterite is formed through annealing of ISM material, the low enstatite-to-forsterite ratio implies a rather porous structure of the amorphous silicates and brief heating events, such as shocks, which prevent the formation of enstatite.

The high-temperature region in the inner disk near the central star is the natural location where crystallization must occur. Assuming that the inner disk region is the sole region where crystalline silicates are formed, the presence of crystalline silicates at low temperatures implies that efficient radial mixing of the processed dust from the inner disk to larger radii must occur. At the early, high-accretion phases of the disk, the transport of angular momentum is expected to efficiently mix material from the hot inner to the cold outer parts of the disk (Bockelée-Morvan et al. 2002; Dullemond et al. 2006). Although at a first glance, this scenario would be able to explain our observations, a strong argument against it is the radial dependency of the crystalline silicate composition. If the crystalline silicates originated from a single formation region before being distributed through the disk, the composition of the processed material would be constant with radius. Indeed, detailed disk models by Gail (2004), which take radial mixing into account and predict the dust composition as a function of radius, show exactly this counterargument. While Gail (2004) predicts that the composition of the crystalline silicates in inner regions of the disk will be dominated by enstatite, which would be consistent with our observations, the radial mixing model also predicts a large mass fraction of enstatite at larger radii, in contradiction with our results. The only way to save the radial mixing scenario is to assume that during the active mixing phase, nonequilibrium conditions prevail in the inner parts of the disk, forming only forsterite. This might be achieved by very rapid outward transportation of the formed forsterite, which would prevent prolonged heating of the grains or substantial gas-solid reactions that could lead to the formation of enstatite. During the passive, low-accretion disk phase, the phase in which we are observing our TTS sample, where radial mixing is not expected to be efficient, equilibrium conditions might be reached again, resulting in the observed large fraction of enstatite in the inner disks. At present, however, there is no theoretical foundation for this scenario.

The alternative model to the radial mixing scenario is the in situ formation of crystalline silicates at radii of about 5–15 AU. As at these distances, stellar radiation cannot heat the dust to sufficiently high temperatures for crystallization to occur, and an alternative heating mechanism is required. A promising model involves the local heating of dust and gas by shock waves (Harker & Desch 2002; Desch et al. 2005). For typical densities and shock speeds, small dust grains should be efficiently heated to high temperatures up to disk radii of about 10 AU. A possible source for the shocks could be gravitational instabilities or planetary-mass companions within the disk. Shock heating could provide sufficiently brief heating events such that equilibrium conditions or prolonged annealing will not occur, preventing the formation of enstatite at larger radii. In the innermost (∼1 AU) disk, due to higher densities as well as heating by the central star, cooling can

be expected to take longer, such that equilibrium conditions can be reached. The suggested overall increase of the forsterite mass fraction in the inner ∼15 AU of the disks might reflect the idea that spiral waves could affect the entire disk region, causing shock to occur over a large range of radii, or simply that the forsterite, produced at 5–15 AU from the central star, is accreted inwards to smaller radii. This shock wave scenario could explain why some systems do not show any evidence for the presence of crystalline silicates at the longest wavelengths, or even at any wavelengths at all (e.g., Kessler-Silacci et al. 2006); these systems might not (yet) have produced disk instabilities or planet-sized objects large enough to produce shock waves.

Ideally, the spatial distribution of the different silicate species should be directly determined by spatially resolved spectroscopy. Due to observational difficulties, this is at present limited to the much brighter HAeBe and the most nearby TTS systems. Using mid-IR interferometric observations obtained with the VLTI/MIDI instrument, van Boekel et al. (2004b) were able, for a sample of HAeBe systems, to spatially separate the contribution to the IR emission coming from the inner ∼2 AU of the disk from that coming from larger radii. These observations clearly showed that the crystalline silicates in the observed HAeBe systems are mainly concentrated in the inner, high-temperature parts of the disk, and that they have a composition consistent with a formation under (near-)equilibrium conditions. However, before concluding that all crystalline silicates form in the inner parts of the disk, one has to realize that the systems studied by van Boekel et al. (2004b) show no crystalline silicate bands or substantially weaker crystalline silicate bands at the longer (20–30 μm) wavelengths in their *Spitzer* and *ISO* spectra (Meeus et al. 2001; J. Bouwman et al. 2008, in preparation). This suggests that these HAeBe systems, in contrast to the disks in our TTS sample, did not witness substantial radial mixing or in situ formation of crystalline silicates at larger radii, as only the innermost regions of the HAeBe disks contain observable quantities of crystalline silicates.

4.3. *PAH Molecules in Disks Surrounding T Tauri Stars*

Although the main focus of this paper is silicate dust processing, we report the tentative detection of emission bands from PAH molecules. Emission bands of PAH molecules are commonly found in environments with a strong UV flux, such as the circumstellar disks around HAeBe stars. As PAH molecules can contain a substantial fraction of the available carbon and are spectroscopically more easily detectable than carbon in larger grains, they can provide us with important clues concerning the carbon chemistry of circumstellar environments. Characterizing the PAH population is also important for understanding the observed gas temperatures in disks, as the stochastically heated molecules strongly influence the temperature through photoelectric heating. Since the gas temperature determines the pressure scale height of the disk, the presence of PAH molecules can therefore have a substantial influence on the disk geometry. Five out of the seven TTS systems of our sample show a band at 8.2 μm, which we identify with emission from PAH molecules. This is the first time this band has been observed in low-mass pre-main-sequence systems. The relatively high fraction of systems in our sample that show evidence for PAH molecules seems to contradict other studies such as the "Cores to Disks" *Spitzer* legacy study by Geers et al. (2006), which found no PAH emission around sources with spectral types later than G8. However, many studies are based on the analysis of the 6.2 and 11.3 μm PAH bands. As already noticed by Peeters et al. (2002), these latter two bands seem to be suppressed in the PAH population producing the 8.2 μm feature. Just based on the 6.2 and 11.3 μm features, we would only have

detected PAH emission in the HD 143006 system, a G6/8-type star, which would be consistent with the conclusions by Geers et al. (2006). Also, as the 8.2 μm feature coincides with the strong amorphous silicate band, one can only make a firm conclusion concerning its presence after carefully modeling the silicate emission bands. The fact that we observe a PAH band at 8.2 μm rather than at the commonly observed band position between 7.7 and 7.9 μm suggests a fundamental difference in carbon chemistry between our sample and the more luminous HAeBe and F- and early G-type TTS systems. At this point, we can only speculate that the difference in carbon chemistry could be linked to differences between the X-ray fluxes or stellar wind properties of intermediate-mass systems and those of low-mass pre-main-sequence stars. If this is the case, it could also influence the possibility and chemical path by which more complex prebiotic organic molecules can be formed in protoplanetary disks.

APPENDIX A

HD 143006

HD 143006 is a well-studied (e.g., Garcia-Lario et al. 1990; Walker & Wolstencroft 1988; Sylvester et al. 1996; Coulson et al. 1998; Natta et al. 2004; Dent et al. 2005) classical T Tauri star of spectral type G6/8 that appears to be a member of the Upper Scorpius OB association (Mamajek et al. 2004). It displays many T Tauri characteristics, including infrared-to-millimeter excess (Odenwald 1986), optical emission lines (Stephenson 1986), and coronal activity revealed through X-rays (Sciortino et al. 1998). It is thus an "old" accretion disk system, with an age of 3–5 Myr.

APPENDIX B

RX J1612.6−1859A

RX J1612.6−1859A and RX J1612.6−1859B are the names assigned in the nomenclature of Martin et al. (1998) to a pair of emission-line sources in the ρ Oph vicinity. The former object is an M0 star, also known as 2MASS J16123916−1859284 or GSC 06209−01312, that has been studied only by optical spectroscopy (Martin et al. 1998; The 1964). The latter object, by contrast, is a well-known T Tauri star, also known as ScoPMS 52 (Walter et al. 1994) or Wa Oph 3 (Walter 1986). This K0 star was, in fact, the target of the FEPS observations and the source discussed in our companion paper (Silverstone et al. 2006) as not having any excess emission out to 8 μm (and indeed not out to 24 μm; Carpenter et al. 2008). For our IRS observations of this source, however, the IRS peak-up routine was centered on to the mid-IR bright object RX J1612.6−1859A in the slit rather than RX J1612.6−1859B, 20$''$ away. The observations discussed herein are thus of RX J1612.6−1859A, an M0 emission-line object.

REFERENCES

Acke, B., & van den Ancker, M. E. 2004, A&A, 426, 151
Acke, B., van den Ancker, M. E., Dullemond, C. P., van Boekel, R., & Waters, L. B. F. M. 2004, A&A, 422, 621
Alcala, J. M., Krautter, J., Schmitt, J. H. M. M., Covino, E., Wichmann, R., & Mundt, R. 1995, A&AS, 114, 109
Apai, D., Pascucci, I., Sterzik, M. F., van der Bliek, N., Bouwman, J., Dullemond, C. P., & Henning, Th. 2004, A&A, 426, L53
Beckwith, S. V. W., Henning, Th., & Nakagawa, Y. 2000, in Protostars and Planets IV, ed. V. Mannings, A. P. Boss, & S. S. Russell (Tucson: Univ. Arizona Press), 533
Beckwith, S. V. W., Sargent, A. I., Chini, R. S., & Guesten, R. 1990, AJ, 99, 924
Begemann, B., Dorschner, J., Henning, Th., Mutschke, H., & Thamm, E. 1994, ApJ, 423, L71
Bell, K. R., Cassen, P. M., Wasson, J. T., & Woolum, D. S. 2000, in Protostars and Planets IV, ed. V. Mannings, A. P. Boss, & S. S. Russell (Tucson: Univ. Arizona Press), 897
Bockelée-Morvan, D., Gautier, D., Hersant, F., Huré, J.-M., & Robert, F. 2002, A&A, 384, 1107
Bohren, C. F., & Huffman, D. R. 1983, Absorption and Scattering of Light by Small Particles (New York: Wiley)
Bouwman, J., de Koter, A., Dominik, C., & Waters, L. B. F. M. 2003, A&A, 401, 577
Bouwman, J., Meeus, G., de Koter, A., Hony, S., Dominik, C., & Waters, L. B. F. M. 2001, A&A, 375, 950
Carpenter, J. M., Mamajek, E. E., Hillenbrand, L. A., & Meyer, M. R. 2006, ApJ, 651, L49
Carpenter, J. M., et al. 2008, ApJ (submitted)
Chiang, E., & Goldreich, P. 1997, ApJ, 490, 368
Coulson, I. M., Walther, D. M., & Dent, W. R. F. 1998, MNRAS, 296, 934

D'Alessio, P., Calvet, N., Hartmann, L., Franco-Hernández, R., & Servín, H. 2006, ApJ, 638, 314
Davis, A. M., & Richter, F. M. 2004, in Treatise on Geochemistry, Vol. 1, ed. A. M. Davis, H. D. Holland, & K. K. Turekian (Amsterdam: Elsevier), 407
Davoisne, C., Djouadi, Z., Leroux, H., D'Hendecourt, L., Jones, A., & Deboffle, D. 2006, A&A, 448, L1
Dent, W. R. F., Greaves, J. S., & Coulson, I. M. 2005, MNRAS, 359, 663
Desch, S. J., Ciesla, F. J., Hood, L. L., & Nakamoto, T. 2005, in ASP Conf. Ser. 341, Chondrites and the Protoplanetary Disk, ed. A. N. Krot, E. R. D. Scott, & B. Reipurth (San Francisco: ASP), 849
de Zeeuw, P. T., Hoogerwerf, R., de Bruijne, J. H. J., Brown, A. G. A., Blaauw, A. 1999, AJ, 117, 354
Dorschner, J., Begemann, B., Henning, Th., Jäger, C., & Mutschke, H. 1995, A&A, 300, 503
Dullemond, C. P., Apai, D., & Walch, S. 2006, ApJ, 640, L67
Dullemond, C. P., & Dominik, C. 2004a, A&A, 417, 159
———. 2004b, A&A, 421, 1075
Dullemond, C. P., Dominik, C., & Natta, A. 2001, ApJ, 560, 957
Dutrey, A., Guilloteau, S., Duvert, G., Prato, L., Simon, M., Schuster, K., & Menard, F. 1996, A&A, 309, 493
Fabian, D., Henning, Th., Jäger, C., Mutschke, H., Dorschner, J., & Wehrhan, O. 2001, A&A, 378, 228
Fabian, D., Jäger, C., Henning, Th., Dorschner, J., & Mutschke, H. 2000, A&A, 364, 282
Furlan, E., et al. 2005, ApJ, 628, L65
———. 2006, ApJS, 165, 568
Gail, H.-P. 2004, A&A, 413, 571
Garcia-Lario, P., Manchado, A., Suso, S. R., Pottasch, S. R., & Olling, R. 1990, A&AS, 82, 497
Geers, V. C., et al. 2006, A&A, 459, 545

Green, J. D., Hartmann, L., Calvet, N., Watson, D. M., Ibrahimov, M., Furlan, E., Sargent, B., & Forrest, W. J. 2006, ApJ, 648, 1099

Hallenbeck, S. L., Nuth, J. A., & Nelson, R. N. 2000, ApJ, 535, 247

Harker, D. E., & Desch, S. J. 2002, ApJ, 565, L109

Henning, Th., Begemann, B., Mutschke, H., & Dorschner, J. 1995, A&AS, 112, 143

Henning, Th., Dullemond, C., Wolf, S., & Dominik, C. 2006, in Planet Formation, ed. H. Klahr & W. Brandner (Cambridge: Cambridge Univ. Press), 113

Henning, Th., & Mutschke, H. 1997, A&A, 327, 743

Henning, Th., Mutschke, H., & Jäger, C. 2005, in IAU Symp. 231, Astrochemistry: Recent Successes and Current Challenges, ed. D. Lis, G. Blake, & E. Herbst (Cambridge: Cambridge Univ. Press), 457

Henning, Th., & Stognienko, R. 1996, A&A, 311, 291

Higdon, S. J. U., et al. 2004, PASP, 116, 975

Houck, J. R., et al. 2004, ApJS, 154, 18

Houk, N., Smith-Moore, M. 1988, in Michigan Spectral Survey (Vol. 4; Ann Arbor: Univ. Michigan)

Jäger, C., Molster, F. J., Dorschner, J., Henning, Th., Mutschke, H., & Waters, L. B. F. M. 1998, A&A, 339, 904

Kemper, F., Vriend, W. J., & Tielens, A. G. G. M. 2005, ApJ, 633, 534

Kenyon, S. J., & Hartmann, L. 1987, ApJ, 323, 714

Kessler-Silacci, J., Hillenbrand, L. A., Blake, G. A., & Meyer, M. R. 2005, ApJ, 622, 404

Kessler-Silacci, J., et al. 2006, ApJ, 639, 275

———. 2007, ApJ, 659, 680

Koike, C., Chihara, H., Tsuchiyama, A., Suto, H., Sogawa, H., & Okuda, H. 2003, A&A, 399, 1101

Koike, C., et al. 2000, A&A, 363, 1115

Lahuis, F., & Boogert, A. 2003, in SFChem 2002: Chemistry as a Diagnostic of Star Formation, ed. C. L. Curry & M. Fich (Ottawa: NRC Press), 335

Leinert, C., et al. 2004, A&A, 423, 537

Li, A., & Draine, B. T. 2002, ApJ, 572, 232

Luhman, K. L. 2008, in ASP Conf Ser., Handbook of Star-Forming Regions, ed. B. Reipurth (San Francisco: ASP), in press

Luhman, K. L., Joergens, V., Lada, C., Muzerolle, J., Pascucci, I., & White, R. 2007, in Protostars and Planets V, ed. B. Reipurth, D. Jewitt, & K. Keil (Tucson: Univ. Arizona Press), 443

Mamajek, E. E., Meyer, M. R., Hinz, P. M., Hoffmann, W. F., Cohen, M., & Hora, J. L. 2004, ApJ, 612, 496

Mamajek, E. E., Meyer, M. R., & Liebert, J. 2002, AJ, 124, 1670

Martin, E. L., Montmerle, T., Gregorio-Hetem, J., & Casanova, S. 1998, MNRAS, 300, 733

Mattioda, A. L., Hudgins, D. M., & Allamandola, L. J. 2005, ApJ, 629, 1188

McCaughrean, M. J., & O'Dell, C. R. 1996, AJ, 111, 1977

Meeus, G., Waters, L., Bouwman, J., van den Ancker, M. E., Waelkens, C., & Malfait, K. 2001, A&A, 365, 476

Men'shchikov, A. B., & Henning, Th. 1997, A&A, 318, 879

Meyer, M. R., et al. 2004, ApJS, 154, 422

———. 2006, PASP, 118, 1690

Min, M., Dominik, C., Hovenier, J. W., de Koter, A., & Waters, L. B. F. M. 2006, A&A, 445, 1005

Min, M., Hovenier, J. W., & de Koter, A. 2005, A&A, 432, 909

Min, M., Waters, L. B. F. M., de Koter, A., Hovenier, J. W., Keller, L. P., & Markwick-Kemper, F. 2007, A&A, 462, 667

Molster, F. J., Demyk, A., D'Hendecourt, L., & Bradley, J. P. 2003, in Lunar and Planetary Inst. Conf. 34, ed. S. Mackwell (Houston: Lunar and Planetary Institute), 1148

Molster, F. J., Waters, L. B. F. M., & Tielens, A. G. G. M. 2002a, A&A, 382, 222

Molster, F. J., Waters, L. B. F. M., Tielens, A. G. G. M., & Barlow, M. J. 2002b, A&A, 382, 184

Natta, A., Testi, L., Calvet, N., Henning, Th., Waters, R., & Wilner, D. 2007, in Protostars and Planets V, ed. B. Reipurth, D. Jewitt, & K. Keil (Tucson: Univ. Arizona Press), 767

Natta, A., Testi, L., Neri, R., Shepherd, D. S., & Wilner, D. J. 2004, A&A, 416, 179

Neuhäuser, R., & Forbrich, J. 2008, in ASP Conf. Ser., Handbook of Star-Forming Regions, ed. B. Reipurth (San Francisco: ASP), in press

Neuhäuser, R., et al. 2000, A&AS, 146, 323

Nomura, H., & Nakagawa, Y. 2006, ApJ, 640, 1099

Odenwald, S. F. 1986, ApJ, 307, 711

Pascucci, I., et al. 2006, ApJ, 651, 1177

Peeters, E., Hony, S., Van Kerckhoven, C., Tielens, A. G. G. M., Allamandola, L. J., Hudgins, D. M., & Bauschlicher, C. W. 2002, A&A, 390, 1089

Petaev, M. I., & Wood, J. A. 2005, in ASP Conf. Ser. 341, Chondrites and the Protoplanetary Disk, ed. A. N. Krot, E. R. D. Scott, & B. Reipurth (San Francisco: ASP), 373

Pollack, J. B., Hubickyj, O., Bodenheimer, P., Lissauer, J., Podolak, M., & Greenzweig, Y. 1996, Icarus, 124, 62

Preibisch, T., Brown, A. G. A., Bridges, T., Guenther, E., & Zinnecker, H. 2002, AJ, 124, 404

Preibisch, T., Guenther, E., Zinnecker, H., Sterzik, M., Frink, S., & Roeser, S. 1998, A&A, 333, 619

Press, W. H., Teukolsky, S. A., Vetterling, W. T., & Flannery, B. P. 1992, Numerical Recipes in FORTRAN. The Art of Scientific Computing (2nd ed.; Cambridge: Cambridge Univ. Press)

Przygodda, F., van Boekel, R., Àbrahàm, P., Melnikov, S. Y., Waters, L. B. F. M., & Leinert, C. 2003, A&A, 412, L43

Quanz, S. P., Henning, Th., Bouwman, J., Ratzka, T., & Leinert, C. 2006, ApJ, 648, 472

Quanz, S. P., Henning, Th., Bouwman, J., van Boekel, R., Juhász, A., Linz, H., Pontoppidan, K. M., & Lahuis, F. 2007, ApJ, 668, 359

Rietmeijer, F. J. M. 1988, in Lunar and Planetary Science Conf. 19 (Cambridge/Houston: Cambridge Univ. Press/LPI), 513

Sargent, B., et al. 2006, ApJ, 645, 395

Schegerer, A., Wolf, S., Voshchinnikov, N. V., Przygodda, F., & Kessler-Silacci, J. E. 2006, A&A, 456, 535

Schräpler, R., & Henning, Th. 2004, ApJ, 614, 960

Sciortino, S., Damiani, F., Favata, F., & Micela, G. 1998, A&A, 332, 825

Servoin, J. L., & Piriou, B. 1973, Phys. Status Solidi B, 55, 677

Silverstone, M., et al. 2006, ApJ, 639, 1138

Sloan, G. C., et al. 2005, ApJ, 632, 956

Stephenson, C. B. 1986, ApJ, 300, 779

Strom, K. M., Strom, S. E., Edwards, S., Cabrit, S., & Skrutskie, M. F. 1989, AJ, 97, 1451

Sylvester, R. J., Skinner, C. J., Barlow, M. J., & Mannings, V. 1996, MNRAS, 279, 915

Thamm, E., Steinacker, J., & Henning, Th. 1994, A&A, 287, 493

The, P.-S. 1964, PASP, 76, 293

Thompson, S. P., Fonti, S., Verrienti, C., Blanco, A., Orofino, V., & Tang, C. 2002, A&A, 395, 705

van Boekel, R., Min, M., Waters, L. B. F. M., de Koter, A., Dominik, C., van den Ancker, M. E., & Bouwman, J. 2005, A&A, 437, 189

van Boekel, R., Waters, L. B. F. M., Dominik, C., Bouwman, J., de Koter, A., Dullemond, C. P., & Paresce, F. 2003, A&A, 400, L21

———. 2004a, A&A, 418, 177

van Boekel, R., et al. 2004b, Nature, 432, 479

van Diedenhoven, B., Peeters, E., Van Kerckhoven, C., Hony, S., Hudgins, D. M., Allamandola, L. J., & Tielens A. G. G. M. 2004, ApJ, 611, 928

Voshchinnikov, N. V., Il'in, V. B., Henning, Th., & Dubkova, D. N. 2006, A&A, 445, 167

Walker, H. J., & Wolstencroft, R. D. 1988, PASP, 100, 1509

Walter, F. M. 1986, ApJ, 306, 573

Walter, F. M., Vrba, F. J., Mathieu, R. D., Brown, A., & Myers, P. C. 1994, AJ, 107, 692

Weidenschilling, S. J. 1997, in ASP Conf. Ser. 122, From Stardust to Planetesimals, ed. Y. J. Pendleton & A. G. G. M. Tielens (San Francisco: ASP), 281

Werner, M. W., et al. 2004, ApJS, 154, 1

Wooden, D. H., Harker, D. E., & Brearley, A. J. 2005, in ASP Conf. Ser. 341, Chondrites and the Protoplanetary Disk, ed. A. N. Krot, E. R. D. Scott, & B. Reipurth (San Francisco: ASP), 774